



Surface state of the interorbital pairing state in the Sr_2RuO_4 superconductor

Satoshi Ando , Satoshi Ikegaya , Shun Tamura, Yukio Tanaka, and Keiji Yada
 Department of Applied Physics, Nagoya University, Nagoya 464-8603, Japan



(Received 12 October 2022; accepted 29 November 2022; published 21 December 2022)

We study the (001) surface state of a recently proposed E_g symmetry interorbital-odd spin-triplet s -wave superconducting (SC) state in Sr_2RuO_4 . We confirm that this pair potential is transformed into a chiral d -wave pair potential and a pseudo-Zeeman field in the band basis for a low-energy range. Because of the chiral d -wave pair potential, the surface states appear near zero energy in the momentum range enclosed by the nodal lines of the chiral d -wave pair potential for each band at the (001) surface. Nevertheless, the pseudo-Zeeman field gives band splitting of the surface states, and its splitting energy is much smaller than the SC energy gap. The local density of states (LDOS) at the (001) surface of the SC state has a pronounced peak structure at zero energy because of the surface states near zero energy when the order of the resolution is lower than the splitting energy. This peak structure is robust against perturbations, such as an orbital Rashba coupling or an E_u SC pair potential at the surface.

DOI: [10.1103/PhysRevB.106.214520](https://doi.org/10.1103/PhysRevB.106.214520)

I. INTRODUCTION

The superconducting (SC) symmetry in Sr_2RuO_4 (SRO) has been a central issue in condensed-matter physics since its discovery [1]. Spin-triplet chiral p -wave ($k_x + ik_y$ wave) was long considered the leading candidate for SC symmetry because of the observations of the constant spin-susceptibility (NMR [2] and neutron scattering [3]) and time-reversal symmetry breaking (TRSB) (μSR [4] and Kerr effect [5]). In addition, numerous theoretical studies have supported the realization of the $k_x + ik_y$ -wave state [6–19]. Recently, however, Pustogow *et al.* [20] pointed out that there had been a heating issue in the previously reported NMR experiment. When this problem was solved, spin susceptibility under an in-plane magnetic field was suppressed at temperatures below T_c in both NMR and μSR measurements [20–23]. These recent results appear to be inconsistent with the $k_x + ik_y$ -wave state. However, ultrasound and thermodynamics experiments suggest multiple degenerate-order parameters [24–26], and several theoretical studies focused on the two-component order parameters with TRSB in SRO have been reported [27–37]. In general, TRSB SC states are composed of two different components that belong to two different irreducible representations (irreps) or to the same irrep. In cases where two different irreps are mixed, the possibility of certain combinations has been proposed, such as $s' + id_{x^2-y^2}$ wave [28], $d_{x^2-y^2} + ig_{xy}(x^2-y^2)$ wave [29–32], and $s + id_{xy}$ wave [33,34]. However, in the same irreps case, the allowed pair symmetry has been reported to be only E_g irrep by Refs. [20–23] in D_{4h} [38]. The most simple basis function of E_g symmetry is the $k_z(k_x + ik_y)$ wave (i.e., the chiral d -wave). However, this simple chiral d -wave pairing forms Cooper pairs between the electrons in different layers of an SRO crystal, which has a nearly two-dimensional electronic structure; therefore, the formation of such Cooper pairs has been considered difficult. Nevertheless, when the orbital degree of freedom

is considered, on-site E_g SC pairing states, which can resolve the aforementioned problems, are possible. Actually, an interorbital-odd spin-triplet s -wave pairing state in the E_g irrep has recently attracted attention [35–37]. This pair has an energy-gap structure similar to that of a chiral d -wave pairing but differs in that it has a Bogoliubov Fermi surface. This state is one of the most promising candidates because it can explain the μSR experiments under both hydrostatic pressure [39] and in-plane uniaxial strain [40].

In this paper, we calculate the dispersion of the surface state and the local density of states (LDOS) at the (001) surface (hereafter referred to as the top surface) of the E_g interorbital SC state by the recursive Green's function formula [41]. The surface states appear near zero energy with splits by a much smaller energy scale than that of the SC gap. The physical origin of this surface state can be understood by an effective low-energy Hamiltonian characterized by an effective chiral d -wave pair potential and a pseudo-Zeeman field. As a result, the LDOS has a pronounced zero-energy peak when the order of the resolution is lower than the splitting energy. This peak structure is robust against perturbations at the top surface, such as an orbital Rashba coupling or a chiral p -wave SC pair potential.

II. ANALYTICAL DESCRIPTION

A. Model Hamiltonian

Let us start with a model Hamiltonian for an interorbital superconducting state of SRO, as originally proposed in Ref. [36]. We focus on the t_{2g} orbitals of the Ru ions (i.e., the d_{yz} , d_{zx} , and d_{xy} orbitals), which dominate the bands near the Fermi level. The corresponding Bogoliubov-de Gennes (BdG) Hamiltonian is given by

$$H = \frac{1}{2} \sum_k \Psi_k^\dagger \tilde{H}(k) \Psi_k \quad (1)$$

with

$$\check{H}(\mathbf{k}) = \begin{pmatrix} \hat{H}_N(\mathbf{k}) & \hat{\Delta}(\mathbf{k}) \\ \hat{\Delta}^\dagger(\mathbf{k}) & -\hat{H}_N^\dagger(-\mathbf{k}) \end{pmatrix}, \quad (2)$$

and

$$\begin{aligned} \Psi_k^\dagger &= (C_k^\dagger, C_{-k}^\dagger), \\ C_k^\dagger &= (c_{k,\uparrow,yz}^\dagger, c_{k,\uparrow,zx}^\dagger, c_{k,\uparrow,xy}^\dagger, c_{k,\downarrow,yz}^\dagger, c_{k,\downarrow,zx}^\dagger, c_{k,\downarrow,xy}^\dagger), \end{aligned} \quad (3)$$

where $c_{k,\sigma,\chi}^\dagger$ creates an electron with momentum \mathbf{k} and spin σ in orbital χ . The normal-state Hamiltonian is described by

$$\begin{aligned} \hat{H}_N(\mathbf{k}) &= \begin{pmatrix} \bar{\xi} + \bar{\lambda}_0 + \bar{\lambda}_3 & \bar{\lambda}_1 + i\bar{\lambda}_2 \\ \bar{\lambda}_1 - i\bar{\lambda}_2 & \bar{\xi} + \bar{\lambda}_0 - \bar{\lambda}_3 \end{pmatrix}, \\ \bar{\xi} &= \begin{pmatrix} \xi_{yz} & 0 & 0 \\ 0 & \xi_{zx} & 0 \\ 0 & 0 & \xi_{xy} \end{pmatrix}, \quad \bar{\lambda}_0 = \begin{pmatrix} 0 & h_{10} & h_{20} \\ h_{10} & 0 & h_{30} \\ h_{20} & h_{30} & 0 \end{pmatrix}, \\ \bar{\lambda}_{j=1,2,3} &= \begin{pmatrix} 0 & -ih_{4j} & -ih_{5j} \\ ih_{4j} & 0 & -ih_{6j} \\ ih_{5j} & ih_{6j} & 0 \end{pmatrix}, \end{aligned} \quad (4)$$

where $\bar{\xi} + \bar{\lambda}_0$ contains the spin-independent hopping integrals and the chemical potentials and $\bar{\lambda}_{j=1,2,3}$ describe the interorbital spin-orbit couplings. The explicit forms of the matrix elements h_{ij} and the corresponding band parameters are summarized in Appendix A. The proposed interorbital pair potential associated with the E_g irrep is denoted by

$$\begin{aligned} \hat{\Delta} &= \begin{pmatrix} 0 & \bar{\Delta} \\ \bar{\Delta} & 0 \end{pmatrix}, \quad \bar{\Delta} = \Delta(\bar{L}_x + i\bar{L}_y), \\ \bar{L}_x &= \begin{pmatrix} 0 & 0 & 0 \\ 0 & 0 & i \\ 0 & -i & 0 \end{pmatrix}, \quad \bar{L}_y = \begin{pmatrix} 0 & 0 & -i \\ 0 & 0 & 0 \\ i & 0 & 0 \end{pmatrix}, \end{aligned} \quad (5)$$

where \bar{L}_x and \bar{L}_y are the orbital angular momentum operators in the orbital space and $\Delta (\geq 0)$ denotes the magnitude of the pair potential. We assume that Δ is constant with respect to \mathbf{k} . The present pair potential describes spin-triplet superconductivity, where the d vector is directed along the c axis of SRO. Notably, this interorbital superconducting state is stabilized by the spin-orbit couplings of h_{53} and h_{63} [36].

B. Approximate low-energy Hamiltonian

In this subsection, we derive an approximate Hamiltonian that enables us to grasp the essential properties of the present model. For this purpose, although we lose quantitative accuracy, we treat the interorbital hybridizations of $\bar{\lambda}_{i=0,1,2,3}$ as the perturbation. On the basis of the second-order perturbation theory, we can deform the Hamiltonian in an approximate band basis as

$$\tilde{u}^\dagger \check{H}(\mathbf{k}) \tilde{u} = \begin{pmatrix} \check{\mathcal{H}}_\alpha & \check{\mathcal{V}}_{\alpha\beta} & \check{\mathcal{V}}_{\alpha\gamma} \\ \check{\mathcal{V}}_{\beta\alpha} & \check{\mathcal{H}}_\beta & \check{\mathcal{V}}_{\beta\gamma} \\ \check{\mathcal{V}}_{\gamma\alpha} & \check{\mathcal{V}}_{\gamma\beta} & \check{\mathcal{H}}_\gamma \end{pmatrix} + O(\lambda^3), \quad (6)$$

with

$$\begin{aligned} \check{\mathcal{H}}_\nu &= \begin{pmatrix} \tilde{\varepsilon}_\nu & \tilde{\psi}_\nu \\ \tilde{\psi}_\nu^\dagger & -\tilde{\varepsilon}_\nu \end{pmatrix}, \\ \tilde{\varepsilon}_\nu &= \varepsilon_\nu \tilde{\sigma}_0, \quad \tilde{\psi}_\nu = \psi_\nu (i\tilde{\sigma}_2), \end{aligned} \quad (7)$$

and

$$\begin{aligned} \check{\mathcal{V}}_{\nu\nu'} &= \begin{pmatrix} 0 & \tilde{\mathcal{D}}_{\nu\nu'} \\ -\tilde{\mathcal{D}}_{\nu\nu'}^* & 0 \end{pmatrix}, \\ \tilde{\mathcal{D}}_{\nu\nu'} &= (\psi_{\nu\nu'} + \mathbf{d}_{\nu\nu'} \cdot \tilde{\sigma})(i\tilde{\sigma}_2), \\ \mathbf{d}_{\nu\nu'} &= (d_{1,\nu\nu'}, d_{2,\nu\nu'}, d_{3,\nu\nu'}), \end{aligned} \quad (8)$$

for $\nu, \nu' = \alpha, \beta$, and γ , where $\tilde{\sigma} = (\tilde{\sigma}_1, \tilde{\sigma}_2, \tilde{\sigma}_3)$ and $\tilde{\sigma}_0$ represent the Pauli matrices and the unit matrix in pseudospin space, respectively, and $O(\lambda^n)$ represents the Landau symbol with respect to the n th order of the matrix elements in $\bar{\lambda}_i$. The explicit forms of the matrix elements and the unitary operator \tilde{u} are given in Appendix B. We construct the unitary matrix \tilde{u} to diagonalize the normal-state Hamiltonian \hat{H}_N within the second-order of $\bar{\lambda}_i$. In addition, the diagonal components of $\varepsilon_\alpha, \varepsilon_\beta$, and ε_γ give the kinetic energies of three different bands, which constitute three separated Fermi surfaces. Thus, the unitary transformation in Eq. (6) changes the basis of the Hamiltonian from the original orbital basis to the approximate band basis. Then, $\psi_{\nu,\nu'} i\tilde{\sigma}_2$ and $\mathbf{d}_{\nu,\nu'} \cdot \tilde{\sigma} i\tilde{\sigma}_2$ ($\mathbf{d}_{\nu,\nu} = \mathbf{0}$) are the spin-singlet and -triplet pair potentials, respectively. Parameters $d_{1,\nu\nu'}$, $d_{2,\nu\nu'}$, and $d_{3,\nu\nu'}$ are the x , y , and z components of the d vector, respectively. These pair potentials have momentum dependence even though the original pair potential does not. To check the validity of this approximation, we show the Fermi surfaces in the approximate band basis and the numerical band basis, which are obtained by the numerical diagonalization of the normal-state Hamiltonian in Figs. 1(a) and 1(b). In Fig. 1, the lattice constant of the conventional unit cell in the in-plane directions and the z direction are represented by a and c , respectively, and c is twice the distance between nearest-neighbor layers. The approximate Fermi surfaces (dotted lines) and the numerical Fermi surfaces (solid lines) nicely correspond. Figure 1(c) shows the numerical Fermi surfaces projected onto the surface Brillouin zone (BZ). The dashed and dotted lines indicate the Fermi surfaces at $k_z c = 0$ and $k_z c = 2\pi$, respectively. As we will show later, the property of the projected Fermi surfaces is related to the emergence of the low-energy surface states at the top surface.

We here proceed with a further approximation to construct a low-energy effective Hamiltonian for each band. According to the argument in Refs. [36,42–44], the low-energy excitation in the vicinity of the Fermi surface of the ν band can be evaluated by

$$\check{\mathcal{H}}_\nu^{\text{eff}} = \check{\mathcal{H}}_\nu + \sum_{\nu' \neq \nu} \frac{\check{\mathcal{V}}_{\nu'\nu}^\dagger \check{\tau}_z \check{\mathcal{V}}_{\nu'\nu}}{\varepsilon_\nu - \varepsilon_{\nu'}}, \quad (9)$$

where $\check{\tau}_z = \text{diag}[1, 1, -1, -1]$. A detailed derivation of Eq. (9) is presented in Appendix B. Eventually, we obtain the low-energy effective Hamiltonian for the ν -band within the second-order perturbation of $\bar{\lambda}_i$,

$$\begin{aligned} \check{\mathcal{H}}_\nu^{\text{eff}} &= \begin{bmatrix} \tilde{h}_\nu(\mathbf{k}) & \tilde{\psi}_\nu(\mathbf{k}) \\ \tilde{\psi}_\nu^\dagger(\mathbf{k}) & -\tilde{h}_\nu^\dagger(-\mathbf{k}) \end{bmatrix}, \\ \tilde{h}_\nu &= (\varepsilon_\nu - \gamma_\nu) \tilde{\sigma}_0 + \mathbf{m}_\nu \cdot \tilde{\sigma}, \end{aligned} \quad (10)$$

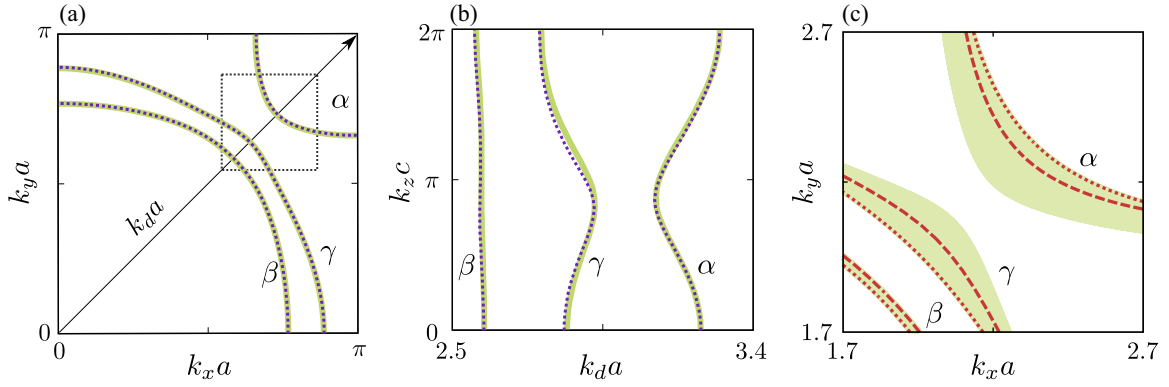


FIG. 1. (a) The Fermi surface at $k_z c = 0$, where the arrow shows the $k_d a$ axis, which is the diagonal line on the $k_x k_y$ plane. (b) The k_z dependence of the Fermi surface on the $k_d a$ line shown in (a). Solid lines are in the approximated band basis, and dotted lines are in the numerical band basis. (c) The numerical Fermi surface projected into the surface Brillouin zone in the range enclosed by the square shown in (a). Dotted and dashed lines show the numerical Fermi surface at $k_z c = 2\pi$ and $k_z c = 0$, respectively.

with

$$\gamma_v = \sum_{v' \neq v} \frac{|\psi_{v'v}|^2 + |\mathbf{d}_{v'v}|^2}{\varepsilon_v - \varepsilon_{v'}}, \quad (11)$$

$$\mathbf{m}_v = \sum_{v' \neq v} \frac{2\text{Re}[\psi_{v'v} \mathbf{d}_{v'v}^*] - i \mathbf{d}_{v'v} \times \mathbf{d}_{v'v}^*}{\varepsilon_v - \varepsilon_{v'}}, \quad (12)$$

where γ_v describes the modulation in the kinetic energy and \mathbf{m}_v represents the pseudo-Zeeman potential.

We now describe the essential properties of the present model, which is clarified using the effective low-energy Hamiltonian $\tilde{\mathcal{H}}_v^{\text{eff}}$. Remarkably, the effective pair potential ψ_v acting on each band can be decomposed as

$$\psi_v = X_v(\mathbf{k}) + iY_v(\mathbf{k}), \quad (13)$$

where the real functions of $X_v(\mathbf{k})$ and $Y_v(\mathbf{k})$ obey

$$\begin{aligned} X_v(-k_x, k_y, k_z) &= X_v(k_x, k_y, -k_z) = -X_v(\mathbf{k}), \\ X_v(k_x, -k_y, k_z) &= X_v(\mathbf{k}), \end{aligned} \quad (14)$$

and

$$\begin{aligned} Y_v(k_x, -k_y, k_z) &= Y_v(k_x, k_y, -k_z) = -Y_v(\mathbf{k}), \\ Y_v(-k_x, k_y, k_z) &= Y_v(\mathbf{k}), \end{aligned} \quad (15)$$

respectively. (See also Eq. (B101) in Appendix B). The pair potential of ψ_v has both real and imaginary parts, where the real (imaginary) part of the pair potential, i.e., X_v (Y_v), is an odd function with respect to k_x (k_y), even function with respect to k_y (k_x), and odd function with respect to k_z . Thus, the pair potential of ψ_v has the symmetry property equivalent to the chiral d -wave gap function, i.e., $\Delta \propto k_z(k_x + ik_y)$. This implies that the effective pair potential ψ_v has chiral d -wave pairing symmetry similar to the $k_z(k_x + ik_y)$ -wave pair potential. The pair potential vanishes at $k_z c = 0$ and $k_z c = 2\pi$. Thus, in the absence of the pseudo-Zeeman potential (i.e., $\mathbf{m}_v = 0$), $\tilde{\mathcal{H}}_v$ exhibits the line nodes at $k_z = 0$ and $k_z c = 2\pi$, where the location of the line nodes corresponds to the dashed and dotted lines in Fig. 1(c). In addition, the pair potential has mirror-odd nature with respect to k_z [i.e., $\psi_v(k_x, k_y, k_z) = -\psi_v(k_x, k_y, -k_z)$], which enables us to expect the formation

of low-energy surface states at the top surface [44–52]. Moreover, it has been already shown that, for a $k_z(k_x + ik_y)$ -wave superconductor, we obtain topologically-protected flat-band zero-energy surface states at the top surface [45,53–55]. More specifically, the relevant topological invariant predicts that the flat-band zero-energy surface states appear at momenta enclosed by the nodal lines in the surface BZ (see also the detailed discussion in Appendix D). Thus, on the basis of the analogy between the $k_z(k_x + ik_y)$ -wave superconductor and the present superconductor characterized by the effective chiral d -wave pair potential, we expect that, if the pseudo-Zeeman potential is absent, flat-band zero-energy surface states will appear in the momentum range enclosed by the dashed and dotted lines in Fig. 1(c). Nevertheless, in the present model, the emergence of the pseudo-Zeeman potential is inevitable. The energy eigenvalue of $\tilde{\mathcal{H}}_v^{\text{eff}}$ is given by

$$\begin{aligned} E_{\pm,s} &= \pm E_{\text{cd}} + s|\mathbf{m}_v|, \\ E_{\text{cd}} &= \sqrt{(\varepsilon_v + \gamma_v)^2 + |\psi_v|^2}, \end{aligned} \quad (16)$$

for $s = \pm$. The pseudo-Zeeman potential clearly shifts the bands of $\pm E_{\text{cd}}$, which originally exhibit the line nodes at momenta satisfying $\varepsilon_v + \gamma_v = 0$ and $|\psi_v| = 0$. In particular, the line nodes in $E_{+,-} = E_{\text{cd}} - |\mathbf{m}_v|$ and $E_{-,+} = -E_{\text{cd}} + |\mathbf{m}_v|$ are inflated to the Bogoliubov-Fermi surfaces by the pseudo-Zeeman field [42,43]. Moreover, we infer that exact flat-band zero-energy surface states can no longer exist because of the energy splitting from the pseudo-Zeeman field. Even so, the energy splitting in the surface states would be substantially smaller than Δ because the pseudo-Zeeman potential $|\mathbf{m}_v|$ is proportional to Δ^2 .

Summarizing the previous discussion, we can expect the present model to display nearly zero-energy surface states at the top surface in the momentum range enclosed by the dashed and dotted lines in Fig. 1(c), where the energy splitting of the surface states is due to the pseudo-Zeeman potential $\mathbf{m}_v \propto \Delta^2$. In the next section, we will confirm this statement by examining the surface energy dispersion and the surface LDOS numerically.

III. DETAILED PROPERTIES OF SURFACE STATES

A. Recursive Green's function techniques

In this section, we consider the open boundary condition in the z direction and the periodic boundary condition in the x and y directions to calculate the surface Green's function for the semi-infinite system. In addition, we consider flat surfaces and do not consider surface reconstructions. Then, the momentum parallel to the surface $\mathbf{k}_{\parallel} \equiv (k_x, k_y)$ becomes a good quantum number, and the problem is reduced to a one-dimensional problem along the z direction at each momentum \mathbf{k}_{\parallel} . The BdG Hamiltonian $\hat{H}(\mathbf{k})$ in Eq. (2) includes interlayer hopping up to the next-nearest layer. Thus, the Hamiltonian of a system with n layers stacked in the z direction can be written as

$$\begin{aligned} H_n(\mathbf{k}_{\parallel}) = & \sum_{j=1}^n \sum_{\alpha, \beta} C_{j, \alpha, \mathbf{k}_{\parallel}}^{\dagger} \{h_0(\mathbf{k}_{\parallel})\}_{\alpha, \beta} C_{j, \beta, \mathbf{k}_{\parallel}} \\ & + \sum_{j=1}^{n-1} \sum_{\alpha, \beta} [C_{j, \alpha, \mathbf{k}_{\parallel}}^{\dagger} \{t_1(\mathbf{k}_{\parallel})\}_{\alpha, \beta} C_{j+1, \beta, \mathbf{k}_{\parallel}} + \text{H.c.}] \\ & + \sum_{j=1}^{n-2} \sum_{\alpha, \beta} [C_{j, \alpha, \mathbf{k}_{\parallel}}^{\dagger} \{t_2(\mathbf{k}_{\parallel})\}_{\alpha, \beta} C_{j+2, \beta, \mathbf{k}_{\parallel}} + \text{H.c.}], \end{aligned} \quad (17)$$

where α and β denote the internal degrees of freedom: spin, orbital, and particle-hole; $C_{j, \alpha, \mathbf{k}_{\parallel}}^{\dagger}$ and $C_{j, \alpha, \mathbf{k}_{\parallel}}$ are the creation and annihilation operators at the j th site in the z direction, respectively, and $h_0(\mathbf{k}_{\parallel})$ and $t_{1(2)}(\mathbf{k}_{\parallel})$ are the intralayer element and the interlayer hopping between the (next) nearest-neighbor layers of the Hamiltonian, respectively.

To obtain the surface Green's function of the top layer, we use the recursive Green's function technique. By formulating the recursion relation using the Möbius transformation, we can calculate the surface Green's function in a semi-finite system [41]. This technique is developed for the system with up to nearest-neighbor hopping, whereas the Hamiltonian in Eq. (17) includes next-nearest-neighbor hopping. Thus, we treat the n -layers system as the n' ($= n/2$)-layers system by treating two adjacent original layers as a single layer. The Green's function of the $2n'$ -layers system is given by $G^{n'}(z, \mathbf{k}_{\parallel}) = [zI - H_{2n'}(\mathbf{k}_{\parallel})]^{-1}$. Then, the (n', n') and $(n' - 1, n' - 1)$ components of the Green's functions $G_{n'}^{n'}$ and $G_{n'-1}^{n'-1}$ satisfy the next equation,

$$G_{n'}^{n'}(z, \mathbf{k}_{\parallel}) = [zI - h(\mathbf{k}_{\parallel}) - t^{\dagger}(\mathbf{k}_{\parallel})G_{n'-1}^{n'-1}(z, \mathbf{k}_{\parallel})t(\mathbf{k}_{\parallel})]^{-1}, \quad (18)$$

where $z = \varepsilon + i\delta$ and I is the unit matrix. Parameter ε is a real frequency, and δ is an infinitesimal imaginary part. Here, $h(\mathbf{k}_{\parallel})$ and $t(\mathbf{k}_{\parallel})$ are given by

$$h = \begin{pmatrix} h_0 & t_1 \\ t_1^{\dagger} & h_0 \end{pmatrix} \quad (19)$$

and

$$t = \begin{pmatrix} t_2 & 0 \\ t_1 & t_2 \end{pmatrix}, \quad (20)$$

respectively. By taking the limit $n' \rightarrow \infty$ with the Möbius transformation, we obtain the top-surface Green's function for the semi-infinite system [41], $\dot{g}^s = \lim_{n' \rightarrow \infty} G_{n'}^{n'}$, where \dot{g}^s is a 24×24 matrix with the orbital, spin, particle-hole, and layer degrees of freedom. The details are given in Appendix C. The energy dispersion of the surface states within the bulk energy gap can be determined by examining the poles of the Green's function. Thus, we can obtain the dispersion of the surface state from the pole of \dot{g}^s . In the same manner, we can obtain the bottom-surface Green's function, $\dot{g}^{s, \text{btm}} = \lim_{n' \rightarrow \infty} G_1^{n'}$ from $G_1^{n'} = [zI - h - tG_2^{n'}t^{\dagger}]^{-1}$. From \dot{g}^s and $\dot{g}^{s, \text{btm}}$, we can obtain the Green's function in the bulk,

$$\dot{g} = (zI - h - t^{\dagger}\dot{g}^st - t\dot{g}^{s, \text{btm}}t^{\dagger})^{-1}. \quad (21)$$

The LDOS of the top surface $N^s(\varepsilon)$ and the DOS of the bulk $N(\varepsilon)$ are given by

$$N^s(\varepsilon) = -1/N \sum_{\mathbf{k}_{\parallel}, i} 1/\pi [\text{Im} \dot{g}_{ii}^s(\mathbf{k}_{\parallel}, \varepsilon)], \quad (22)$$

$$N(\varepsilon) = -1/N \sum_{\mathbf{k}_{\parallel}, i} 1/\pi [\text{Im} \dot{g}_{ii}(\mathbf{k}_{\parallel}, \varepsilon)], \quad (23)$$

respectively. Here, we take the summation of i within the electron part in the one layer. Parameter N is the number of sites in the xy plane.

B. Surface energy spectrum

First, we consider the energy dispersion on the diagonal direction of the surface BZ. We choose Δ to be the same order of T_c in SRO. $\Delta = |t_z^{(xy, xy)} \times 10^{-4}|$, where $t_z^{(xy, xy)} = -262.4$ meV is an interlayer hopping parameter shown in Appendix A. Figures 2(a)–2(c) show the dispersion of the surface states by the solid lines and the continuous energy levels in the bulk by the shaded areas for the α , β , and γ bands, respectively. The surface states at the momentum between the points where the SC gap closes are very close to zero energy [56]. In addition, the surface states are not exactly at zero energy, as shown in Figs. 2(d)–2(f), when viewed at a higher energy resolution. Parameters $\delta E_{\alpha, \beta, \gamma}$ in Figs. 2(d)–2(f) show the width of the band splitting at each representative point on the $k_d a$ line for the α , β , and γ bands, respectively. As shown in Fig. 3, the Δ dependence of $\delta E_{\alpha, \beta, \gamma}$ is proportional to Δ^2 . We demonstrate that the presence of nearly zero-energy surface states is due to the effective chiral d -wave-symmetry pair potential, whereas the tiny energy splitting proportional to Δ^2 is inevitable because of the pseudo-Zeeman potential, as shown in the previous section.

C. Surface local density of states

Second, we calculate momentum-resolved LDOS at $\varepsilon = 0$, $-1/\pi \sum_i \text{Im} \dot{g}_{ii}^s(\mathbf{k}_{\parallel}, 0)$. Figures 4(a), 4(e), and 4(i) show color plots of the momentum-resolved LDOS in the range shown in Fig. 1(c). In Figs. 4(a–d), 4(e–h), and 4(i–l), we choose $\delta = \Delta \times 10^{-2}$, $\Delta \times 10^{-5}$, and $\Delta \times 10^{-7}$, respectively. The parameter of δ characterizes the resolution of the LDOS with respect to the energy; roughly speaking, the variations in the LDOS within the energy range of δ are smeared. Figures 4(b)–4(d), 4(f)–4(h), and 4(j)–4(l) show enlarged maps surrounded by the squares in Figs. 4(a), 4(e), and 4(i), respectively. The

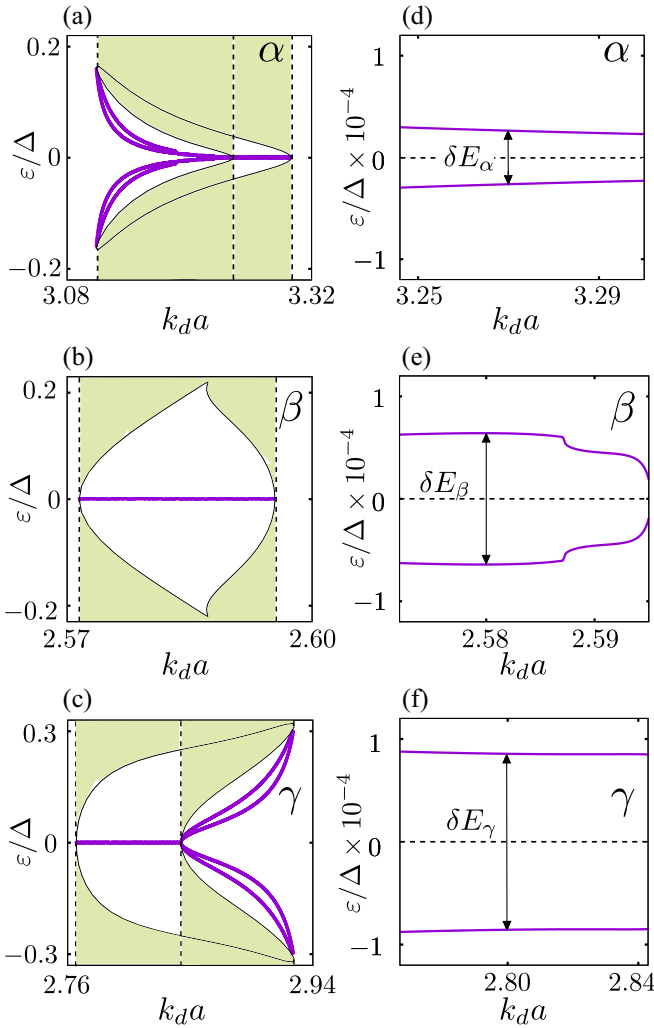


FIG. 2. The surface states in the (a) α , (b) β , and (c) γ bands. Solid lines are the surface state, and shaded areas are the continuous energy levels in the bulk. The surface states between the dotted and dashed lines are shown in Fig. 1(c) in a tiny energy range for (d) α , (e) β , and (f) γ bands. $\delta E_{\alpha,\beta,\gamma}$ are the width of the band splitting at $k_da = 3.27, 2.58, 2.80$.

dotted and dashed lines show projected Fermi surface at $k_z c = 0$ and $k_z c = 2\pi$ onto the surface BZ, respectively. For $\delta = \Delta \times 10^{-2}$, the spectral weight increases at the momenta between the dotted and dashed lines for the β and γ bands. The spectral weight for the α band is weaker than those for the other bands. One reason for this weak spectral weight might be the longer localization length of the surface state due to the smaller bulk energy gap in the momentum range enclosed by the dotted and dashed lines for this band. Even outside the enclosed range, a weak spectral weight is observed near the dashed line. This spectral weight arises from the inner-gap surface states outside of the enclosed momentum range, whose energy dispersion becomes closer to zero energy as the momenta approaches the dashed lines, as shown in Fig. 2(a). The γ band also has the inner-gap surface states outside the enclosed momentum range, as shown in Fig. 2(c). However, these surface states are further from the zero energy than those of the α band. When δ is set to a value

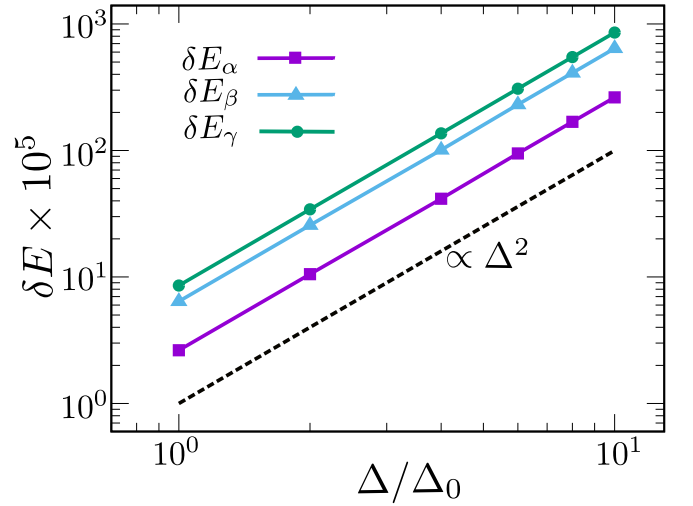


FIG. 3. Common logarithm plot of the Δ dependence of $\delta E_{\alpha,\beta,\gamma}$ shown in Figs. 2(d)–2(f). The dotted line is proportional to Δ^2 . $\Delta_0 = |t_z^{(xy,xy)} \times 10^{-4}|$.

close to the splitting energy scale shown in Figs. 2(d)–2(f), the obtained spectral weight inside the momentum range enclosed by the dotted and dashed lines clearly increases in each band in Figs. 4(e)–4(h). For δ values much smaller than the splitting energy scale, the spectral weight at zero energy becomes weaker, as shown in Figs. 4(i)–4(l), because no surface states exist within the energy range less than δ , as shown in Figs. 2(d)–2(f).

Figures 5(a) and 5(b) show the DOS of the bulk and the LDOS at the top surface, respectively, where we take $\Delta = |t_z^{(xy,xy)} \times 10^{-4}|$ and $\delta = \Delta \times 10^{-2}$. The DOS and the LDOS are normalized by those values at the Fermi energy in the normal state denoted by N_n and N_n^s , respectively. As a result of the momentum-resolved LDOS for $\varepsilon = 0$ shown in Fig. 4(a), a pronounced peak structure appears in the LDOS of the top surface at $\varepsilon = 0$, in contrast to the V-shaped structure in the DOS of the bulk. As we have explained, the surface state is not exactly at zero energy. Therefore, if we take a sufficiently small δ to distinguish the surface state energy level shown in Figs. 2(d)–2(f), the peak structure splits. However, such a small resolution is challenging in actual experiments.

D. E_u -symmetry perturbations

Finally, we study the stability of the zero-energy peak of the LDOS against the perturbations due to inversion symmetry breaking, which is inevitable near the surface; such perturbations include orbital Rashba coupling that induces the Rashba-type spin-orbit coupling through the $L \cdot S$ coupling [57,58] or an E_u symmetry SC pair potential. For the former case, we introduce the orbital Rashba coupling described by

$$\hat{H}_{\text{so}} = 2t_{\text{so}}(\bar{L}_y \bar{\sigma}_0 \sin(k_x a) + \bar{L}_x \bar{\sigma}_0 \sin(k_y a)) \quad (24)$$

at the top surface. This coupling originates from the hopping integral due to the shift of the oxygen sites. In the bulk, O and Ru atoms are on the same plane due to the balance of forces from the upper and lower planes. On the other hand, on the (001) surface, only the force from the lower planes acts, so the

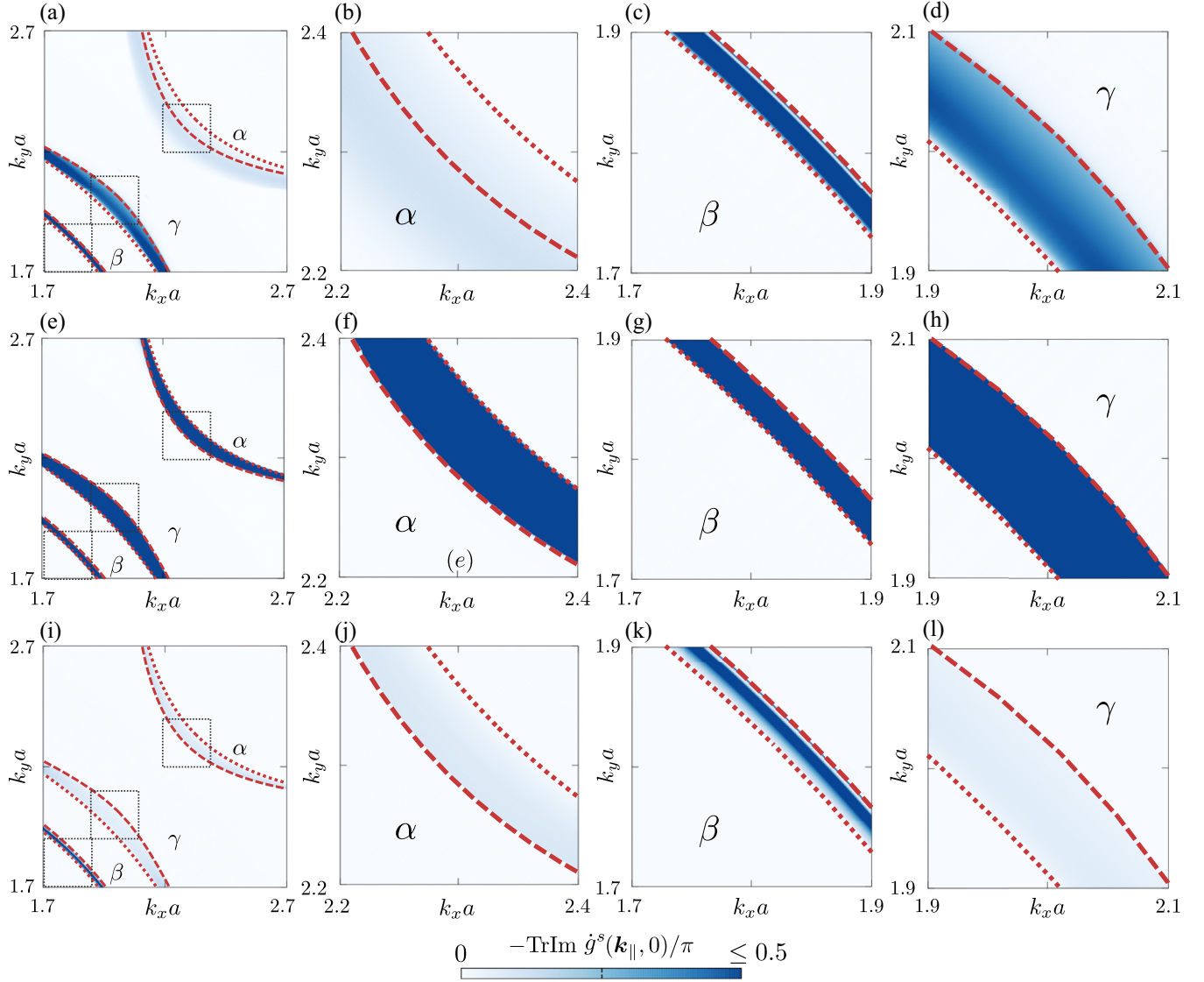


FIG. 4. The momentum-resolved LDOS at $\varepsilon = 0$ in the momentum range shown in Fig. 1(c) for (a) $\delta = \Delta \times 10^{-2}$, (e) $\delta = \Delta \times 10^{-5}$, and (i) $\delta = \Delta \times 10^{-7}$. [(b)–(d), (f)–(h), (j)–(l)] Enlarged maps for (a), (e), and (i) for each band in the range surrounded by the squares, respectively. Dotted and dashed lines show the Fermi surface at $k_z c = 2\pi$ and $k_z c = 0$, respectively.

z coordinates of O and Ru are different due to the difference in bonding strength. Then, the coupling between $p_x - (p_y -)$ orbitals in oxygens and the $yz - (xz -)$ orbital arises along the $x - (y -)$ direction. The resulting effective hopping in t_{2g} subspace has the form given in Eq. (24) as explained in Ref. [58]. We assume that those induced coupling at the surface is much smaller than the original coupling between $p_x - (p_y -)$ orbitals in oxygens and $xy -$ orbital. Therefore, we set t_{s0} to approximately one-tenth the value of $t_x^{(xy, xy)}$. The obtained LDOS is shown in Fig. 6. As evident in this figure, the zero-energy peak remains under this range of t_{s0} . We confirm that the energy levels of the nearly zero-energy surface states do not change against this term. However, its peak height is suppressed, possibly because the localized position of the surface state moves farther into the interior of the crystal. For the latter case, we introduce the chiral E_u SC pair potential at the top surface instead of the E_g interorbital

SC pair potential. The dependence of the LDOS on the pair potential and the gap amplitude are shown in Appendix E. Here, we set the amplitude of the gap as the order of T_c . In this case, the change of the resultant LDOS in Fig. 9 is too small for them to be distinguished from the original ones given in Fig. 5(b).

IV. DISCUSSION

In scanning tunneling microscopy (STM) observations of the top surface of SRO [59,60], the differential conductance spectrum shows a V-shaped structure rather than a zero-bias peak structure, which appears to contradict the presence of nearly zero-energy surface states. Therefore, at face value, the interorbital E_g SC state seems to be excluded by the STM observations. Nevertheless, we also remark several concerns for making the definitive conclusion.

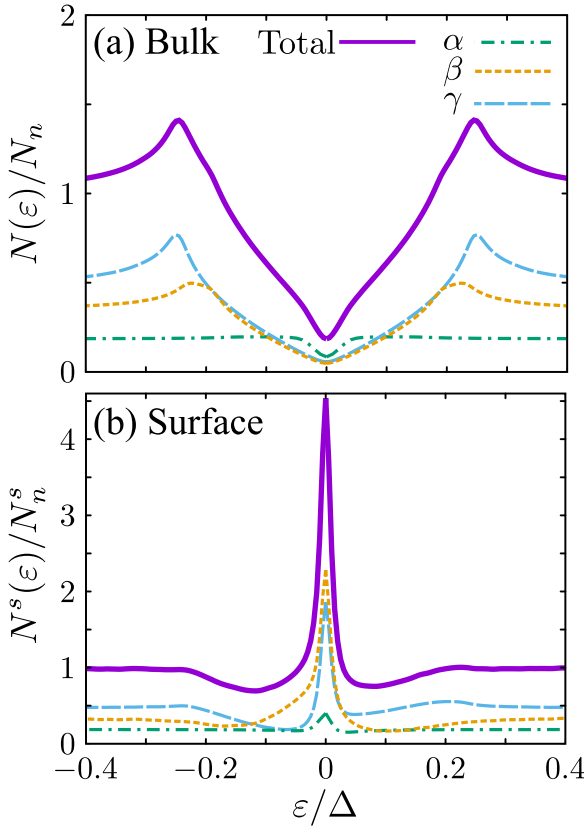


FIG. 5. (a) The DOS of the bulk and each band's contribution to the DOS. (b) The LDOS at the top surface and each band's contribution to the LDOS.

First, we have only considered the clean surfaces preserving \mathbf{k}_{\parallel} as a good quantum number. In actual experiments, surface roughness would inevitably break translational symmetry. When the surface roughness is substantial, for a $k_z(k_x + ik_y)$ -wave superconductor, the zero-energy surface states at the top surface are highly vulnerable [61]. In addition, in some experiments, surface reconstruction breaking fourfold rotation symmetry at the top surface of SRO has been ob-

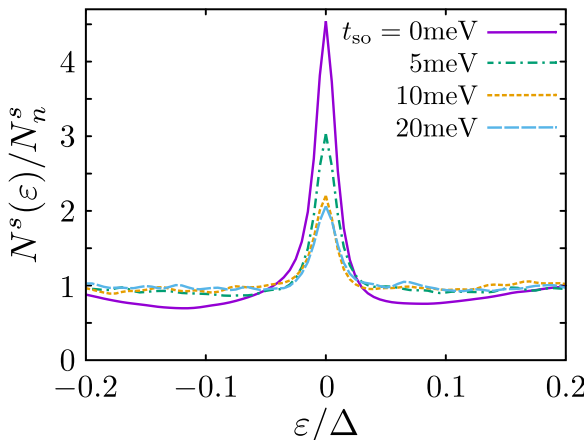


FIG. 6. The t_{so} dependence of the LDOS under the orbital Rashba coupling at the top surface.

served [39,62,63]. Thus, examining the effect of surface roughness/reconstruction on the surface states of the present model would be an important future task.

Second, structure of the tip may affect observations of the differential conductance. Actually, a junction consisting of a *one-dimensional* normal-metal lead wire and a two-dimensional d_{xy} -wave superconductor has been shown to exhibit a V-shaped conductance spectrum even in the presence of flat-band zero-energy surface states at the junction interface [64–70]. In general, this V-shaped spectrum is due to the sign change in the pair potential with respect to the momentum parallel to the surface; that is,

$$\Delta_{d_{xy}}(k_x, k_y) = -\Delta_{d_{xy}}(k_x, -k_y),$$

where $\Delta_{d_{xy}} \propto k_x k_y$ with $k_{x(y)}$ representing momentum perpendicular (parallel) to the interface. More specifically, the Andreev reflection at the junction interface is substantially suppressed because of the destructive interference between the transmission channels feeling $\Delta_{d_{xy}}(k_x, k_y)$ and that feeling $\Delta_{d_{xy}}(k_x, -k_y) = -\Delta_{d_{xy}}(k_x, k_y)$. In the present model, the effective pair potential satisfies

$$\psi_v(\mathbf{k}_{\parallel}, k_z) = -\psi_v(-\mathbf{k}_{\parallel}, k_z), \quad (25)$$

where \mathbf{k}_{\parallel} corresponds to the momentum parallel to the top surface. Thus, as in the case of one-dimensional normal-metal/two-dimensional d_{xy} -wave superconductor junctions, the Andreev reflection between the STM tip and SRO top surface may be significantly suppressed owing to the similar destructive interference. To resolve this stalemate, microscopic studies on the transport properties of the present model are strongly desired.

Summarizing above discussion, the STM results of the top surface of SRO [59,60] appears inconsistent with the interorbital E_g SC state in SRO. Nevertheless, to be more conclusive, microscopic studies on the effects of surface roughness/reconstruction and the destructive interference of the Andreev reflection in STM measurements are highly desired. Importantly, other candidate states in SRO, such as $s' + id_{x^2-y^2}$ wave [28], $d_{x^2-y^2} + ig_{xy}(x^2-y^2)$ wave [29–32], and $s + id_{xy}$ wave [33,34] have two-dimensional nature (i.e., their pair potential are insensitive to k_z), while mirror-odd nature of the pair potential with respect to k_z is responsible for the emergence of zero-energy surface states at the (001) surface [45,46,49] (see also Appendix D). Namely, we cannot expect the zero-energy peak structure in the top surface LDOS except for the interorbital E_g SC state. As a result, tunneling spectroscopy with suppressed surface roughness/reconstruction and with large junction area enables us to distinguish the interorbital E_g SC state from other candidate states conclusively.

We also remark that several theoretical papers have argued the difficulty of the interorbital E_g SC state in SRO owing to the necessity of large Hund's coupling and large interlayer spin-orbit coupling [71,72]. Nonetheless, interorbital pairings can be realized with the help of the electron-phonon interaction [56], which is not considered explicitly in Refs. [71,72]. Investigating the interorbital E_g SC state in the system including the electron-phonon interaction is an important future work.

V. SUMMARY AND CONCLUSIONS

We have studied the surface state of the interorbital-odd spin-triplet s -wave pairing at the (001) surface in SRO. We have demonstrated the presence of nearly zero-energy surface states due to the effective chiral d -wave symmetry pair potential, whereas the tiny energy splitting proportional to Δ^2 is inevitable because of the pseudo-Zeeman potential. As a result, the surface LDOS exhibits a pronounced zero-energy peak when the order of the resolution is lower than the splitting energy shown in Figs. 2(d)–2(f). We have also shown that the zero-energy peak is robust against perturbations due to inversion symmetry breaking at the surface, such as the orbital Rashba coupling and the E_u symmetry pair potential.

ACKNOWLEDGMENTS

This work was supported by Scientific Research (A) (KAKENHI Grant No. JP20H00131), and Scientific Research (B) (KAKENHI Grant No. JP20H01857). S.I. is supported by a Grant-in-Aid for JSPS Fellows (JSPS KAKENHI Grant No. JP21J00041). This work was supported by JSPS Core-to-Core Program (No. JPJSCCA20170002). S.A. would like to take this opportunity to thank the Nagoya University Interdisciplinary Frontier Fellowship supported by Nagoya University and JST, the establishment of university fellowships towards the creation of science technology innovation, Grant No. JPMJFS2120.

APPENDIX A: MODEL HAMILTONIAN OF THREE-DIMENSIONAL Sr_2RuO_4 IN THE NORMAL STATE

We describe the three-dimensional Hamiltonian of Sr_2RuO_4 (SRO) in the normal state [36],

$$\hat{H}_N(\mathbf{k}) = \sum_{lj} h_{lj}(\mathbf{k}) \bar{\lambda}_l \otimes \tilde{\sigma}_j. \quad (\text{A1})$$

The Gell-Mann matrices $\bar{\lambda}_{l=0-8}$ are defined by

$$\begin{aligned} \bar{\lambda}_0 &= \begin{pmatrix} 1 & 0 & 0 \\ 0 & 1 & 0 \\ 0 & 0 & 1 \end{pmatrix}, \quad \bar{\lambda}_1 = \begin{pmatrix} 0 & 1 & 0 \\ 1 & 0 & 0 \\ 0 & 0 & 0 \end{pmatrix}, \\ \bar{\lambda}_2 &= \begin{pmatrix} 0 & 0 & 1 \\ 0 & 0 & 0 \\ 1 & 0 & 0 \end{pmatrix}, \quad \bar{\lambda}_3 = \begin{pmatrix} 0 & 0 & 0 \\ 0 & 0 & 1 \\ 0 & 1 & 0 \end{pmatrix}, \\ \bar{\lambda}_4 &= \begin{pmatrix} 0 & -i & 0 \\ i & 0 & 0 \\ 0 & 0 & 0 \end{pmatrix}, \quad \bar{\lambda}_5 = \begin{pmatrix} 0 & 0 & -i \\ 0 & 0 & 0 \\ i & 0 & 0 \end{pmatrix}, \\ \bar{\lambda}_6 &= \begin{pmatrix} 0 & 0 & 0 \\ 0 & 0 & -i \\ 0 & i & 0 \end{pmatrix}, \quad \bar{\lambda}_7 = \begin{pmatrix} 1 & 0 & 0 \\ 0 & -1 & 0 \\ 0 & 0 & 0 \end{pmatrix}, \\ \bar{\lambda}_8 &= \frac{1}{\sqrt{3}} \begin{pmatrix} 1 & 0 & 0 \\ 0 & 1 & 0 \\ 0 & 0 & -2 \end{pmatrix}. \end{aligned}$$

$h_{lj}(\mathbf{k})$ are

$$h_{00}(\mathbf{k}) = \frac{1}{3} [\xi_{yz}(\mathbf{k}) + \xi_{zx}(\mathbf{k}) + \xi_{xy}(\mathbf{k})], \quad (\text{A2})$$

$$h_{70}(\mathbf{k}) = \frac{1}{2} [\xi_{yz}(\mathbf{k}) - \xi_{zx}(\mathbf{k})], \quad (\text{A3})$$

$$h_{80}(\mathbf{k}) = \frac{1}{2\sqrt{3}} [\xi_{yz}(\mathbf{k}) + \xi_{zx}(\mathbf{k}) - 2\xi_{xy}(\mathbf{k})], \quad (\text{A4})$$

$$\begin{aligned} h_{10}(\mathbf{k}) &= g(\mathbf{k}) \\ &= -4t_{xy}^z \sin k_x \sin k_y \\ &\quad - 4t_{xxy}^z (\sin 2k_x \sin k_y + \sin k_x \sin 2k_y) \\ &\quad + 8t_z^z \sin \frac{k_x a}{2} \sin \frac{k_y a}{2} \cos \frac{k_z c}{2}, \end{aligned} \quad (\text{A5})$$

$$h_{20}(\mathbf{k}) = 8t_z^{(zx,xy)} \sin \frac{k_x a}{2} \sin \frac{k_y a}{2} \cos \frac{k_z c}{2}, \quad (\text{A6})$$

$$h_{30}(\mathbf{k}) = 8t_z^{(zx,xy)} \sin \frac{k_x a}{2} \cos \frac{k_y a}{2} \sin \frac{k_z c}{2}, \quad (\text{A7})$$

$$h_{43}(\mathbf{k}) = -\lambda^{\text{SOC}}, \quad (\text{A8})$$

$$h_{52}(\mathbf{k}) = -h_{61}(\mathbf{k}) = \lambda^{\text{SOC}}, \quad (\text{A9})$$

$$h_{51}(\mathbf{k}) = -h_{62}(\mathbf{k}) = 4\lambda_{5162}^{\text{SOC}} \sin k_x a \sin k_y a, \quad (\text{A10})$$

$$h_{52}(\mathbf{k}) = h_{61}(\mathbf{k}) = 2\lambda_{5261}^{\text{SOC}} (\cos k_x a - \cos k_y a), \quad (\text{A11})$$

$$h_{41}(\mathbf{k}) = 8\lambda_{12z}^{\text{SOC}} \sin \frac{k_x a}{2} \sin \frac{k_y a}{2} \cos \frac{k_z c}{2}, \quad (\text{A12})$$

$$h_{42}(\mathbf{k}) = 8\lambda_{12z}^{\text{SOC}} \sin \frac{k_x a}{2} \cos \frac{k_y a}{2} \sin \frac{k_z c}{2}, \quad (\text{A13})$$

$$h_{63}(\mathbf{k}) = -8\lambda_{56z}^{\text{SOC}} \sin \frac{k_x a}{2} \sin \frac{k_y a}{2} \cos \frac{k_z c}{2}, \quad (\text{A14})$$

$$h_{53}(\mathbf{k}) = 8\lambda_{56z}^{\text{SOC}} \sin \frac{k_x a}{2} \cos \frac{k_y a}{2} \sin \frac{k_z c}{2}, \quad (\text{A15})$$

with

$$\begin{aligned} \xi_{yz} &= 2t_y^{(z,z)} \cos k_x a + 2t_x^{(z,z)} \cos k_y a - \mu_z \\ &\quad + 4t_{xy}^{(z,z)} \cos k_x a \cos k_y a \\ &\quad + 2t_{yy}^{(z,z)} \cos 2k_x a + 2t_{xx}^{(z,z)} \cos 2k_y a \\ &\quad + 4t_{xyy}^{(z,z)} \cos 2k_x a \cos k_y a + 4t_{xxy}^{(z,z)} \cos 2k_y a \cos k_x a \\ &\quad + 8t_z^{(z,z)} \cos \frac{k_x a}{2} \cos \frac{k_y a}{2} \cos \frac{k_z c}{2} \\ &\quad + 2t_{zz}^{(z,z)} (\cos k_z c - 1), \end{aligned} \quad (\text{A16})$$

$$\begin{aligned} \xi_{zx} &= 2t_x^{(z,z)} \cos k_x a + 2t_y^{(z,z)} \cos k_y a - \mu_z \\ &\quad + 4t_{xy}^{(z,z)} \cos k_x a \cos k_y a \\ &\quad + 2t_{xx}^{(z,z)} \cos 2k_x a + 2t_{yy}^{(z,z)} \cos 2k_y a \\ &\quad + 4t_{xxy}^{(z,z)} \cos 2k_x a \cos k_y a + 4t_{xyy}^{(z,z)} \cos 2k_y a \cos k_x a \\ &\quad + 8t_z^{(z,z)} \cos \frac{k_x a}{2} \cos \frac{k_y a}{2} \cos \frac{k_z c}{2} \\ &\quad + 2t_{zz}^{(z,z)} (\cos k_z c - 1), \end{aligned} \quad (\text{A17})$$

TABLE I. Parameters for the normal state of the Hamiltonian. The unit is meV.

$t_x^{(z,z)} = -362.4$	$t_y^{(z,z)} = -134$	$t_x^{(xy,xy)} = -262.4$
$t_{xy}^{(z,z)} = -44.01$	$t_{xx}^{(z,z)} = -1.021$	$t_{yy}^{(z,z)} = -5.727$
$t_{xx}^{(xy,xy)} = 34.23$	$t_{xy}^{(xy,xy)} = 16.25$	$t_{xy}^{(z,z)} = -13.93$
$t_{xy}^{(z,z)} = -7.52$	$t_{xx}^{(xy,xy)} = 8.069$	$t_{xy}^{(z,z)} = 3.94$
$\lambda_{\text{SOC}} = 57.39$	$\mu_z = 438.5$	$\mu_{xy} = 218.6$
$t_z^{(z,z)} = -0.0228$	$t_z^{(xy,xy)} = 1.811$	$t_z^z = 9.975$
$t_z^{(zx,xy)} = 8.304$	$t_z^{(z,z)} = 2.522$	$t_z^{(xy,xy)} = -3.159$
$t_{xy}^{(xy,xy)} = -43.72$	$\lambda_{56z}^{\text{SOC}} = -1.247$	$\lambda_{12z}^{\text{SOC}} = -3.576$
$\lambda_{5162}^{\text{SOC}} = -1.008$	$\lambda_{5261}^{\text{SOC}} = 0.3779$	

$$\begin{aligned}
 \xi_{xy} = & 2t_x^{(xy,xy)}(\cos k_x a + \cos k_y a) - \mu_{xy} \\
 & + 4t_{xy}^{(xy,xy)} \cos k_x a \cos k_y a \\
 & + 2t_{xx}^{(xy,xy)}(\cos 2k_y a + \cos 2k_x a) \\
 & + 4t_{xxy}^{(xy,xy)}(\cos 2k_x a \cos k_y a + \cos k_x a \cos 2k_y a) \\
 & + 8t_z^{(xy,xy)} \cos \frac{k_x a}{2} \cos \frac{k_y a}{2} \cos \frac{k_z c}{2} \\
 & + 2t_{zz}^{(xy,xy)}(\cos 2k_z c - 1).
 \end{aligned} \quad (\text{A18})$$

We set the parameters as shown in Table I [36].

APPENDIX B: EFFECTIVE LOW-ENERGY MODEL

In this Appendix, we derive a low-energy Hamiltonian of SRO given by Eq. (10) in the main text. For this purpose, we first deform the BdG Hamiltonian in an approximate band-basis [see Eq. (6) in the main text]. Then, we construct a low-energy effective Hamiltonian for each band by following Refs. [43,44].

In principle, the Hamiltonian in the band basis is obtained by employing a unitary operator that diagonalizes the normal Hamiltonian \hat{H}_N . In this paper, owing to the difficulty of the exact diagonalization, we alternatively utilize a perturbation theory to diagonalize \hat{H}_N approximately. As a preliminary step, we remove all degeneracy in the diagonal part of \hat{H}_N at the Fermi level as shown in Fig. 7(a). We now define a unitary

operator,

$$\hat{u}_p = \hat{u}_1 \hat{u}_2. \quad (\text{B1})$$

The first component of the unitary operator, i.e., \hat{u}_1 , is defined by

$$\hat{u}_1 = \begin{pmatrix} \bar{u}_1 & 0 \\ 0 & \bar{u}_1^* \end{pmatrix}, \quad (\text{B2})$$

$$\bar{u}_1 = \begin{pmatrix} a_1 & -b_1^* & 0 \\ b_1 & a_1 & 0 \\ 0 & 0 & 1 \end{pmatrix}, \quad (\text{B3})$$

with

$$a_1 = \frac{P_1 + R_1}{\sqrt{2P_1(P_1 + R_1)}}, \quad (\text{B4})$$

$$b_1 = \frac{h_{10} + ih_{43}}{\sqrt{2P_1(P_1 + R_1)}}, \quad (\text{B5})$$

$$R_1 = (\xi_{yz} + \xi_{zx})/2, \quad (\text{B6})$$

$$P_1 = \sqrt{R_1^2 + h_{10}^2 + h_{43}^2}. \quad (\text{B7})$$

By applying \hat{u}_1 to \hat{H}_N , we obtain

$$\hat{H}'_N = \hat{u}_1^\dagger \hat{H}_N \hat{u}_1. \quad (\text{B8})$$

The diagonal components of \hat{H}'_N are given by

$$\varepsilon'_1 = Q_1 + P_1, \quad (\text{B9})$$

$$\varepsilon'_2 = Q_1 - P_1, \quad (\text{B10})$$

$$\varepsilon'_3 = \xi_{yz}, \quad (\text{B11})$$

with

$$Q_1 = (\xi_{yz} - \xi_{zx})/2. \quad (\text{B12})$$

By using the unitary transformation of \hat{u}_1 , the degeneracy between ξ_{yz} and ξ_{zx} at the Fermi level is lifted as shown in Fig. 7(b). The second component of \hat{u}_p , i.e., \hat{u}_2 , is defined by

$$\hat{u}_2 = \begin{pmatrix} \bar{a}_2 & -\bar{b}_2^* \\ \bar{b}_2 & \bar{a}_2 \end{pmatrix}, \quad (\text{B13})$$

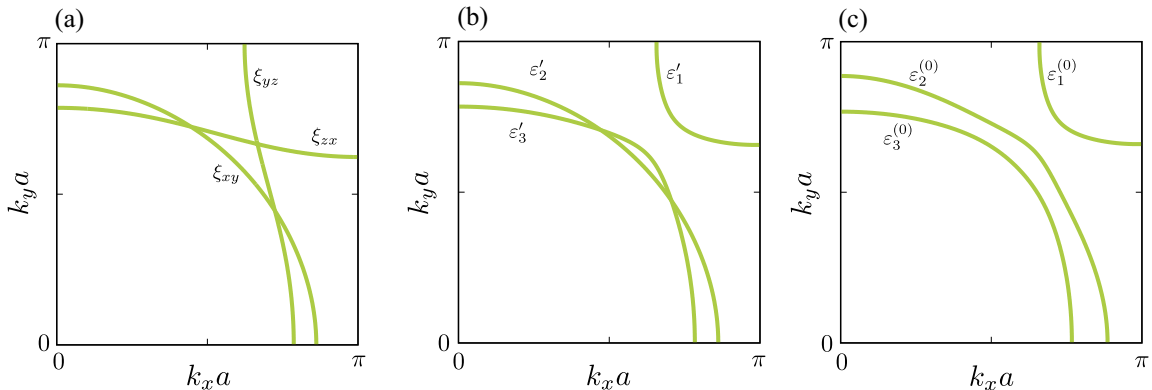


FIG. 7. (a) ξ_{yz} , ξ_{zx} , ξ_{xy} at $k_z = 0$ at the Fermi energy. (b) ε'_1 , ε'_2 , and ε'_3 at $k_z = 0$ at the Fermi energy. (c) $\varepsilon_1^{(0)}$, $\varepsilon_2^{(0)}$, and $\varepsilon_3^{(0)}$ at $k_z = 0$ at the Fermi energy.

$$\bar{a}_2 = \begin{pmatrix} a_2 & 0 & 0 \\ 0 & 1 & 0 \\ 0 & 0 & a_2 \end{pmatrix}, \quad (\text{B14})$$

$$\bar{b}_2 = \begin{pmatrix} 0 & 0 & b_2 \\ 0 & 1 & 0 \\ b_2 & 0 & 0 \end{pmatrix}, \quad (\text{B15})$$

with

$$a_2 = \frac{P_2 + R_2}{\sqrt{2P_2(P_2 + R_2)}}, \quad (\text{B16})$$

$$b_2 = \frac{-g_{52} + ig_{51}}{\sqrt{2P_1(P_1 + R_1)}}, \quad (\text{B17})$$

$$R_2 = (\varepsilon'_1 - \varepsilon'_3)/2, \quad (\text{B18})$$

$$P_2 = \sqrt{R_2^2 + g_{51}^2 + g_{52}^2}, \quad (\text{B19})$$

$$g_{51} = \frac{(P_1 + R_1)h_{51} + h_{10}h_{61} - h_{43}h_{62}}{\sqrt{2P_1(P_1 + R_1)}}, \quad (\text{B20})$$

$$g_{52} = \frac{(P_1 + R_1)h_{52} + h_{10}h_{62} + h_{43}h_{61}}{\sqrt{2P_1(P_1 + R_1)}}. \quad (\text{B21})$$

By applying \hat{u}_2 to \hat{H}'_N , we obtain

$$\hat{h}_p = \hat{u}_2^\dagger \hat{H}'_N \hat{u}_2 = \hat{\varepsilon}^{(0)} + \hat{\eta}, \quad (\text{B22})$$

with

$$\hat{\varepsilon}^{(0)} = \begin{pmatrix} \bar{\varepsilon}^{(0)} & 0 \\ 0 & \bar{\varepsilon}^{(0)} \end{pmatrix}, \quad (\text{B23})$$

$$\hat{\eta} = \begin{pmatrix} \bar{\eta}_0 + \bar{\eta}_3 & \bar{\eta}_1 - i\bar{\eta}_2 \\ \bar{\eta}_1 + i\bar{\eta}_2 & \bar{\eta}_0 - \bar{\eta}_3 \end{pmatrix}, \quad (\text{B24})$$

with

$$\bar{\varepsilon}^{(0)} = \begin{pmatrix} \varepsilon_1^{(0)} & 0 & 0 \\ 0 & \varepsilon_2^{(0)} & 0 \\ 0 & 0 & \varepsilon_3^{(0)} \end{pmatrix}, \quad (\text{B25})$$

$$\bar{\eta}_0 = \begin{pmatrix} 0 & \eta_{10} & \eta_{20} \\ \eta_{10} & 0 & \eta_{30} \\ \eta_{20} & \eta_{30} & 0 \end{pmatrix}, \quad (\text{B26})$$

$$\bar{\eta}_3 = \begin{pmatrix} 0 & -i\eta_{43} & -i\eta_{53} \\ i\eta_{43} & 0 & -i\eta_{63} \\ i\eta_{53} & i\eta_{63} & 0 \end{pmatrix}, \quad (\text{B27})$$

$$\bar{\eta}_{j=1,2} = \begin{pmatrix} 0 & -i\eta_{4j} & 0 \\ i\eta_{4j} & 0 & -i\eta_{6j} \\ 0 & i\eta_{6j} & 0 \end{pmatrix}. \quad (\text{B28})$$

The diagonal components of \hat{h}_p is given by

$$\varepsilon_1^{(0)} = Q_2 + P_2, \quad (\text{B29})$$

$$\varepsilon_2^{(0)} = Q_1 - P_1, \quad (\text{B30})$$

$$\varepsilon_3^{(0)} = Q_2 - P_2, \quad (\text{B31})$$

with

$$Q_2 = (\varepsilon'_1 + \varepsilon'_3)/2. \quad (\text{B32})$$

The remained degeneracy between ε'_2 and ε'_3 is lifted by \hat{u}_2 as shown in Fig. 7(c). The off-diagonal components of \hat{h}_p are given by

$$\eta_{10} = \frac{g_{51}g_{61} + g_{52}g_{62}}{\sqrt{2P_2(P_2 + R_2)}}, \quad (\text{B33})$$

$$\eta_{20} = g_{20}, \quad (\text{B34})$$

$$\eta_{30} = \frac{(P_2 + R_2)g_{30} + g_{51}g_{41} - g_{52}g_{42}}{\sqrt{2P_2(P_2 + R_2)}}, \quad (\text{B35})$$

$$\eta_{43} = \frac{-g_{51}g_{62} + g_{52}g_{61}}{\sqrt{2P_2(P_2 + R_2)}}, \quad (\text{B36})$$

$$\eta_{53} = g_{53}, \quad (\text{B37})$$

$$\eta_{63} = \frac{(P_2 + R_2)g_{30} + g_{51}g_{41} - g_{52}g_{42}}{\sqrt{2P_2(P_2 + R_2)}}, \quad (\text{B38})$$

$$\eta_{41} = \frac{(P_2 + R_2)g_{41} - g_{51}g_{30} - g_{52}g_{63}}{\sqrt{2P_2(P_2 + R_2)}}, \quad (\text{B39})$$

$$\eta_{42} = \frac{(P_2 + R_2)g_{42} - g_{51}g_{63} - g_{52}g_{30}}{\sqrt{2P_2(P_2 + R_2)}}, \quad (\text{B40})$$

$$\eta_{61} = \frac{(P_2 + R_2)g_{61}}{\sqrt{2P_2(P_2 + R_2)}}, \quad (\text{B41})$$

$$\eta_{62} = \frac{(P_2 + R_2)g_{62}}{\sqrt{2P_2(P_2 + R_2)}}, \quad (\text{B42})$$

with

$$g_{20} = \frac{(P_1 + R_1)h_{20} - h_{10}h_{30} - h_{43}h_{63}}{\sqrt{2P_1(P_1 + R_1)}}, \quad (\text{B43})$$

$$g_{30} = \frac{(P_1 + R_1)h_{30} - h_{10}h_{20} - h_{43}h_{53}}{\sqrt{2P_1(P_1 + R_1)}}, \quad (\text{B44})$$

$$g_{4j} = h_{4j}, \quad (\text{B45})$$

$$g_{53} = \frac{(P_1 + R_1)h_{53} + h_{10}h_{63} + h_{43}h_{30}}{\sqrt{2P_1(P_1 + R_1)}}, \quad (\text{B46})$$

$$g_{63} = \frac{(P_1 + R_1)h_{63} - h_{10}h_{53} + h_{43}h_{20}}{\sqrt{2P_1(P_1 + R_1)}}, \quad (\text{B47})$$

$$g_{61} = \frac{(P_1 + R_1)h_{61} - h_{10}h_{51} - h_{43}h_{52}}{\sqrt{2P_1(P_1 + R_1)}}, \quad (\text{B48})$$

$$g_{62} = \frac{(P_1 + R_1)h_{62} - h_{10}h_{52} + h_{43}h_{51}}{\sqrt{2P_1(P_1 + R_1)}}. \quad (\text{B49})$$

In short, all degeneracy at the Fermi level is lifted by the unitary transformation of \hat{u}_p , i.e.,

$$\hat{u}_p^\dagger \hat{H}_N \hat{u}_p = \hat{h}_p = \hat{\varepsilon}^{(0)} + \hat{\eta}. \quad (\text{B50})$$

For the BdG Hamiltonian, the corresponding unitary transformation is represented by

$$\check{H}_p = \check{u}_p^\dagger \check{H} \check{u}_p = \begin{pmatrix} \hat{h}_p(\mathbf{k}) & \hat{\Delta}_p(\mathbf{k}) \\ \hat{\Delta}_p^\dagger(\mathbf{k}) & -\hat{h}_p^\dagger(-\mathbf{k}) \end{pmatrix} \quad (\text{B51})$$

with

$$\check{u}_p = \check{u}_1 \check{u}_2, \quad (\text{B52})$$

$$\check{u}_1 = \begin{pmatrix} \hat{u}_1 & 0 \\ 0 & \hat{u}_1^* \end{pmatrix}, \quad (\text{B53})$$

$$\check{u}_2 = \begin{pmatrix} \hat{u}_2 & 0 \\ 0 & \hat{u}_2^* \end{pmatrix}, \quad (\text{B54})$$

where the pair potential in this basis is given as

$$\hat{\Delta}_p = \begin{pmatrix} -\bar{f}_1 + i\bar{f}_2 & \bar{f}_3 + \bar{f}_0 \\ \bar{f}_3 - \bar{f}_0 & \bar{f}_1 + i\bar{f}_2 \end{pmatrix}, \quad (\text{B55})$$

with

$$\bar{f}_3 = \begin{pmatrix} 0 & 0 & f_{3,13} \\ 0 & 0 & if_{3,23} \\ -f_{3,13} & -if_{3,23} & 0 \end{pmatrix}, \quad (\text{B56})$$

$$\bar{f}_0 = \begin{pmatrix} 0 & 0 & f_{0,13} \\ 0 & 0 & -if_{0,23} \\ \bar{f}_{0,13} & -if_{0,23} & 0 \end{pmatrix}, \quad (\text{B57})$$

$$\bar{f}_{j=1,2} = \begin{pmatrix} 0 & f_{j,12} & 0 \\ -f_{j,12} & 0 & 0 \\ 0 & 0 & 0 \end{pmatrix}, \quad (\text{B58})$$

with

$$f_{j,12} = \Delta(\phi_{j,12} + i\chi_{j,12}), \quad (\text{B59})$$

$$f_{3,13} = \Delta(\phi_{3,13} + i\chi_{3,13}), \quad (\text{B60})$$

$$f_{3,23} = \Delta(\phi_{3,23} + i\chi_{3,23}), \quad (\text{B61})$$

$$f_{0,13} = \Delta\phi_{0,13}, \quad (\text{B62})$$

$$f_{0,23} = \Delta\phi_{0,23}, \quad (\text{B63})$$

with

$$\phi_{1,12} = \frac{h_{10}g_{52} - h_{43}g_{51}}{\sqrt{2P_1(P_1 + R_1)}\sqrt{2P_2(P_2 + R_2)}}, \quad (\text{B64})$$

$$\chi_{1,12} = \frac{(P_1 + R_1)g_{52}}{\sqrt{2P_1(P_1 + R_1)}\sqrt{2P_2(P_2 + R_2)}}, \quad (\text{B65})$$

$$\phi_{2,12} = \frac{-h_{10}g_{51} - h_{42}g_{52}}{\sqrt{2P_1(P_1 + R_1)}\sqrt{2P_2(P_2 + R_2)}}, \quad (\text{B66})$$

$$\chi_{2,12} = \frac{(P_1 + R_1)g_{51}}{\sqrt{2P_1(P_1 + R_1)}\sqrt{2P_2(P_2 + R_2)}}, \quad (\text{B67})$$

$$\phi_{3,13} = \frac{P_1 + R_1}{\sqrt{2P_1(P_1 + R_1)}\sqrt{2P_2(P_2 + R_2)}}, \quad (\text{B68})$$

$$\chi_{3,13} = \frac{(P_1 + R_1)g_{52}}{\sqrt{2P_1(P_1 + R_1)}\sqrt{2P_2(P_2 + R_2)}}, \quad (\text{B69})$$

$$\phi_{3,23} = \frac{(P_1 + R_1)(P_2 + R_2)}{\sqrt{2P_1(P_1 + R_1)}\sqrt{2P_2(P_2 + R_2)}}, \quad (\text{B70})$$

$$\chi_{3,23} = \frac{(P_2 + R_2)h_{10}}{\sqrt{2P_1(P_1 + R_1)}\sqrt{2P_2(P_2 + R_2)}}, \quad (\text{B71})$$

$$\phi_{0,13} = \frac{h_{43}}{\sqrt{2P_1(P_1 + R_1)}}, \quad (\text{B72})$$

$$\phi_{0,23} = \frac{(P_2 + R_2)h_{43}}{\sqrt{2P_1(P_1 + R_1)}\sqrt{2P_2(P_2 + R_2)}}. \quad (\text{B73})$$

For later convenience, we additionally apply a unitary transformation,

$$\check{\mathcal{H}}_q = \check{u}_q^\dagger \check{\mathcal{H}}_p \check{u}_q = \begin{pmatrix} \hat{h}_q(\mathbf{k}) & \hat{\Delta}_q(\mathbf{k}) \\ \hat{\Delta}_q^\dagger(\mathbf{k}) & -\hat{h}_q^\dagger(-\mathbf{k}) \end{pmatrix}, \quad (\text{B74})$$

with

$$\check{u}_q = \begin{pmatrix} \hat{u}_q & 0 \\ 0 & \hat{u}_q \end{pmatrix}, \quad (\text{B75})$$

$$\hat{u}_q = \begin{pmatrix} 1 & 0 & 0 & 0 & 0 & 0 \\ 0 & 0 & 0 & 0 & 1 & 0 \\ 0 & 0 & 1 & 0 & 0 & 0 \\ 0 & 1 & 0 & 0 & 0 & 0 \\ 0 & 0 & 0 & 1 & 0 & 0 \\ 0 & 0 & 0 & 0 & 0 & 1 \end{pmatrix}. \quad (\text{B76})$$

For the normal part,

$$\hat{h}_q = \hat{\varepsilon}_q^{(0)} + \hat{\eta}_q, \quad (\text{B77})$$

with

$$\hat{\varepsilon}_q^{(0)} = \begin{pmatrix} \varepsilon_1^{(0)}\tilde{\sigma}_0 & 0 & 0 \\ 0 & \varepsilon_2^{(0)}\tilde{\sigma}_0 & 0 \\ 0 & 0 & \varepsilon_3^{(0)}\tilde{\sigma}_0 \end{pmatrix}, \quad (\text{B78})$$

$$\hat{\eta}_q = \begin{pmatrix} 0 & \hat{\eta}_{12} & \hat{\eta}_{13} \\ \hat{\eta}_{21} & 0 & \hat{\eta}_{23} \\ \hat{\eta}_{31} & \hat{\eta}_{32} & 0 \end{pmatrix}, \quad (\text{B79})$$

with

$$\hat{\eta}_{ij} = \begin{pmatrix} \eta_{0,ij} + i\eta_{3,ij} & \eta_{1,ij} - i\eta_{2,ij} \\ \eta_{1,ij} + i\eta_{2,ij} & \eta_{0,ij} - i\eta_{3,ij} \end{pmatrix}, \quad (\text{B80})$$

where

$$\eta_{\alpha,ij} = (\tilde{\eta}_\alpha)_{ij}. \quad (\text{B81})$$

For the pair potential part,

$$\hat{\Delta}_q = \begin{pmatrix} 0 & \hat{\Delta}_{12} & \hat{\Delta}_{13} \\ \hat{\Delta}_{21} & 0 & \hat{\Delta}_{23} \\ \hat{\Delta}_{31} & \hat{\Delta}_{32} & 0 \end{pmatrix}, \quad (\text{B82})$$

with

$$\hat{\Delta}_{ij} = \begin{pmatrix} -\Delta_{1,ij} + i\Delta_{2,ij} & \Delta_{3,ij} + \Delta_{0,ij} \\ \Delta_{3,ij} - \Delta_{0,ij} & \Delta_{1,ij} + i\Delta_{2,ij} \end{pmatrix}, \quad (\text{B83})$$

where

$$\Delta_{\alpha,ij} = (\tilde{f}_\alpha)_{ij}. \quad (\text{B84})$$

To proceed the approximate diagonalization of \hat{H}_N , we now consider a perturbation theory with assuming $\hat{\eta}$ as a perturbation. The unperturbed term $\hat{\varepsilon}^{(0)}$ satisfies

$$\hat{u}_1^{(0)} = \begin{pmatrix} \tilde{\sigma}_0 & 0 & 0 \\ 0 & 0 & 0 \\ 0 & 0 & 0 \end{pmatrix}, \quad \hat{u}_2^{(0)} = \begin{pmatrix} 0 & 0 & 0 \\ 0 & \tilde{\sigma}_0 & 0 \\ 0 & 0 & 0 \end{pmatrix},$$

$$\hat{u}_3^{(0)} = \begin{pmatrix} 0 & 0 & 0 \\ 0 & 0 & 0 \\ 0 & 0 & \tilde{\sigma}_0 \end{pmatrix}, \quad (\text{B85})$$

$$\hat{\varepsilon}^{(0)}\hat{u}_j^{(0)} = \varepsilon_j^{(0)}\hat{u}_j^{(0)}. \quad (\text{B86})$$

where $\varepsilon_j^{(0)}$ for $j = 1, 2, 3$ have no degeneracy at the Fermi level. Thus, on the basis of the perturbation theory, we can

diagonalize the perturbed Hamiltonian \hat{h}_q within the second order of $\hat{\eta}$ as

$$\begin{aligned} \hat{\varepsilon} &= \hat{u}_r^\dagger \hat{h}_q \hat{u}_r \\ &= \begin{pmatrix} (\varepsilon_1^{(0)} + \mu_{\lambda,1})\tilde{\sigma}_0 & 0 & 0 \\ 0 & (\varepsilon_2^{(0)} + \mu_{\lambda,2})\tilde{\sigma}_0 & 0 \\ 0 & 0 & (\varepsilon_3^{(0)} + \mu_{\lambda,3})\tilde{\sigma}_0 \end{pmatrix} \\ &\quad + \mathcal{O}(\eta^3), \end{aligned} \quad (\text{B87})$$

where

$$\mu_{\lambda,i} = \sum_{k \neq i} \frac{|\eta_{0,ki}|^2 + |\eta_{ki}|^2}{(\varepsilon_i^{(0)} - \varepsilon_k^{(0)})}. \quad (\text{B88})$$

The last term of Eq. (B87), i.e., $\mathcal{O}(\eta^n)$, represents the Landau symbol with respect to the n th order of the matrix elements in $\hat{\eta}_q$. The unitary transformation \hat{u}_r given by

$$\hat{u}_r = \hat{u}_1 + \hat{u}_2 + \hat{u}_3 = \hat{1} + \hat{W} + \hat{Z}, \quad (\text{B89})$$

with

$$\hat{W} = \begin{pmatrix} 0 & \hat{W}_{12} & \hat{W}_{13} \\ \hat{W}_{21} & 0 & \hat{W}_{23} \\ \hat{W}_{31} & \hat{W}_{32} & 0 \end{pmatrix}, \quad (\text{B90})$$

$$\hat{Z} = \begin{pmatrix} \hat{Z}_{11} & \hat{Z}_{12} & \hat{Z}_{13} \\ \hat{Z}_{21} & \hat{Z}_{22} & \hat{Z}_{23} \\ \hat{Z}_{31} & \hat{Z}_{32} & \hat{Z}_{33} \end{pmatrix}, \quad (\text{B91})$$

where

$$\hat{W}_{ij} = \frac{\hat{\eta}_{ij}}{\varepsilon_j^{(0)} - \varepsilon_i^{(0)}}, \quad (\text{B92})$$

$$\hat{Z}_{ii} = -\frac{1}{2} \sum_{j \neq i} \frac{\hat{\eta}_{ji}^\dagger \hat{\eta}_{ji}}{(\varepsilon_j^{(0)} - \varepsilon_i^{(0)})^2}, \quad (\text{B93})$$

$$\hat{Z}_{ij} = \sum_{l \neq j,i} \frac{\hat{\eta}_{il} \hat{\eta}_{lj}}{(\varepsilon_j^{(0)} - \varepsilon_i^{(0)})(\varepsilon_j^{(0)} - \varepsilon_l^{(0)})}. \quad (\text{B94})$$

As a result, we can deform the BdG Hamiltonian in the approximate band basis as

$$\check{\mathcal{H}}_r = \check{u}_r^\dagger \check{\mathcal{H}}_r \check{u}_r = \begin{pmatrix} \hat{\varepsilon}(\mathbf{k}) & \hat{\mathcal{D}}(\mathbf{k}) \\ \hat{\mathcal{D}}^\dagger(\mathbf{k}) & -\hat{\varepsilon}^T(-\mathbf{k}) \end{pmatrix}, \quad (\text{B95})$$

with

$$\check{u}_r = \begin{pmatrix} \hat{u}_r & 0 \\ 0 & \hat{u}_r^* \end{pmatrix}, \quad (\text{B96})$$

where

$$\hat{\mathcal{D}} = \begin{pmatrix} \hat{\mathcal{D}}_{11} & \hat{\mathcal{D}}_{12} & \hat{\mathcal{D}}_{13} \\ \hat{\mathcal{D}}_{21} & \hat{\mathcal{D}}_{22} & \hat{\mathcal{D}}_{23} \\ \hat{\mathcal{D}}_{31} & \hat{\mathcal{D}}_{32} & \hat{\mathcal{D}}_{33} \end{pmatrix}, \quad (\text{B97})$$

with

$$\hat{\mathcal{D}}_{ij} = \hat{\Delta}_{ij} + \sum_{k \neq i,j} (-\hat{W}_{ik} \hat{\Delta}_{kj} + \hat{\Delta}_{ik} \hat{W}_{kj}^*) + \mathcal{O}(\eta^2). \quad (\text{B98})$$

We can expand $\hat{\mathcal{D}}_{ij}$ as

$$\hat{\mathcal{D}}_{ij} = \begin{pmatrix} d_{1,ij} - id_{2,ij} & -d_{3,ij} + \psi_{ij} \\ -d_{3,ij} - \psi_{ij} & -d_{1,ij} - id_{2,ij} \end{pmatrix}, \quad (\text{B99})$$

where $d_{\alpha,ij}$ are the interband spin-triplet pair potential, and ψ_{ij} are the inter- and intraband spin-singlet pair potential. It should be noted that intraband pair potential is composed only of the spin-singlet pair potential, i.e.,

$$\begin{aligned} \hat{\mathcal{D}}_{ii} &= \begin{pmatrix} 0 & \psi_i \\ -\psi_i & 0 \end{pmatrix}, \\ \psi_i &= \psi_{ii}, \end{aligned} \quad (\text{B100})$$

where

$$\begin{aligned} \psi_1 &= 2\Delta \left(-\frac{\eta_{41}\chi_{1,12} + \eta_{42}\chi_{2,12}}{\varepsilon_1^{(0)} - \varepsilon_2^{(0)}} - \frac{\eta_{20}\phi_{0,13} - \eta_{53}\chi_{3,13}}{\varepsilon_3^{(0)} - \varepsilon_1^{(0)}} \right) \\ &\quad + i2\Delta \left(\frac{\eta_{41}\phi_{1,12} + \eta_{42}\phi_{2,12}}{\varepsilon_1^{(0)} - \varepsilon_2^{(0)}} - \frac{\eta_{53}\phi_{3,13}}{\varepsilon_3^{(0)} - \varepsilon_1^{(0)}} \right), \\ \psi_2 &= 2\Delta \left(\frac{\eta_{41}\chi_{1,12} + \eta_{42}\chi_{1,12}}{\varepsilon_1^{(0)} - \varepsilon_2^{(0)}} - \frac{\eta_{63}\phi_{3,23}}{\varepsilon_2^{(0)} - \varepsilon_3^{(0)}} \right) \\ &\quad + i2\Delta \left(-\frac{\eta_{41}\phi_{1,12} + \eta_{42}\phi_{2,12}}{\varepsilon_1^{(0)} - \varepsilon_2^{(0)}} - \frac{\eta_{30}\phi_{0,23} + \eta_{63}\chi_{3,23}}{\varepsilon_2^{(0)} - \varepsilon_3^{(0)}} \right), \\ \psi_3 &= 2\Delta \left(\frac{\eta_{20}\phi_{0,13} - \eta_{53}\chi_{3,13}}{\varepsilon_3^{(0)} - \varepsilon_1^{(0)}} + \frac{\eta_{63}\phi_{3,23}}{\varepsilon_2^{(0)} - \varepsilon_3^{(0)}} \right) \\ &\quad + i2\Delta \left(\frac{\eta_{30}\phi_{0,23} + \eta_{63}\chi_{3,23}}{\varepsilon_2^{(0)} - \varepsilon_3^{(0)}} + \frac{\eta_{53}\phi_{3,13}}{\varepsilon_3^{(0)} - \varepsilon_1^{(0)}} \right), \end{aligned} \quad (\text{B101})$$

as also discussed in Eqs. (13)–(15). We note that all components of $\hat{\mathcal{D}}_{ij}$ are proportional to Δ . For later convenience, we additionally apply a unitary transformation,

$$\check{\mathcal{H}}_s = \check{u}_s^\dagger \check{\mathcal{H}}_r \check{u}_s = \begin{pmatrix} \check{\mathcal{H}}_\alpha & \check{\mathcal{V}}_{\alpha\beta} & \check{\mathcal{V}}_{\alpha\gamma} \\ \check{\mathcal{V}}_{\beta\alpha} & \check{\mathcal{H}}_\beta & \check{\mathcal{V}}_{\beta\gamma} \\ \check{\mathcal{V}}_{\gamma\alpha} & \check{\mathcal{V}}_{\gamma\beta} & \check{\mathcal{H}}_\gamma \end{pmatrix}, \quad (\text{B102})$$

with

$$\check{u}_s = \begin{pmatrix} \tilde{\sigma}_0 & 0 & 0 & 0 & 0 & 0 \\ 0 & 0 & 0 & 0 & 0 & \tilde{\sigma}_0 \\ 0 & 0 & \tilde{\sigma}_0 & 0 & 0 & 0 \\ 0 & \tilde{\sigma}_0 & 0 & 0 & 0 & 0 \\ 0 & 0 & 0 & 0 & 0 & \tilde{\sigma}_0 \\ 0 & 0 & 0 & \tilde{\sigma}_0 & 0 & 0 \end{pmatrix}, \quad (\text{B103})$$

where

$$\check{\mathcal{H}}_\nu = \begin{pmatrix} \varepsilon_\nu \tilde{\sigma}_0 & \psi_\nu i\tilde{\sigma}_y \\ -\psi_\nu^* i\tilde{\sigma}_y & -\varepsilon_\nu \tilde{\sigma}_0 \end{pmatrix}, \quad (\text{B104})$$

$$\check{\mathcal{V}}_{\nu\nu'} = \begin{pmatrix} 0 & \hat{\mathcal{D}}_{\nu\nu'} \\ -\hat{\mathcal{D}}_{\nu\nu'}^* & 0 \end{pmatrix}. \quad (\text{B105})$$

The notations ν and ν' represent α , β , or γ . The unitary operator \check{u} in Eq. (6) of the main text is defined by

$$\check{u} = \check{u}_p \check{u}_q \check{u}_r \check{u}_s. \quad (\text{B106})$$

Next, we construct a 4×4 low-energy effective Hamiltonian for each band by following Refs. [43,44]. The Green's function corresponding to $\tilde{\mathcal{H}}_s$ is defined by

$$\tilde{G}_s = (\omega \tilde{I} - \tilde{\mathcal{H}}_s)^{-1} \quad (\text{B107})$$

where the Green's function of the (ν, ν) component is given by

$$\begin{aligned} \tilde{G}_\nu^{-1}(\mathbf{k}, \omega) &= \omega \tilde{I} - \tilde{H}_\nu \\ &\quad - (\tilde{\mathcal{V}}_{\nu'\nu}^\dagger \tilde{\mathcal{V}}_{\nu''\nu}^\dagger) \left(\begin{array}{cc} \omega \tilde{I} - \tilde{\mathcal{H}}_{\nu'} & 0 \\ 0 & \omega \tilde{I} - \tilde{\mathcal{H}}_{\nu''} \end{array} \right)^{-1} \\ &\quad \times \left(\begin{array}{c} \tilde{\mathcal{V}}_{\nu'\nu} \\ \tilde{\mathcal{V}}_{\nu''\nu} \end{array} \right) + \mathcal{O}(\mathcal{V}^4) \\ &= \omega \tilde{I} - \tilde{\mathcal{H}}_\nu^{\text{eff}}(\omega) + \mathcal{O}(\mathcal{V}^4), \end{aligned} \quad (\text{B108})$$

where

$$\tilde{\mathcal{H}}_\nu^{\text{eff}}(\omega) = \tilde{\mathcal{H}}_\nu + \sum_{\nu' \neq \nu} \tilde{\mathcal{V}}_{\nu'\nu}^\dagger (\omega \tilde{I} - \tilde{\mathcal{H}}_{\nu'})^{-1} \tilde{\mathcal{V}}_{\nu'\nu}. \quad (\text{B109})$$

We only focus on the low-energy excitation around the Fermi surface of the ν band, where $\varepsilon_\nu \approx 0$ is satisfied. In addition, we assume that the ν and ν' bands lie energetically far from the Fermi surfaces of the ν band, which enables us to ignore the effect of the pair potential on the dispersion of ε'_ν and ε''_ν around at $\varepsilon_\nu \approx 0$. As a result, we can further approximate $\tilde{\mathcal{H}}_\nu^{\text{eff}}(\omega)$ as

$$\tilde{\mathcal{H}}_\nu^{\text{eff}} = \tilde{\mathcal{H}}_\nu + \sum_{\nu' \neq \nu} \frac{\tilde{\mathcal{V}}_{\nu'\nu}^\dagger \tilde{\mathcal{V}}_{\nu'\nu}}{\varepsilon_\nu - \varepsilon_{\nu'}}, \quad (\text{B110})$$

which represent the effective Hamiltonian we consider [43,44], $\tilde{\mathcal{V}}_z = \text{diag}[1, 1, -1, -1]$. The similar argument for constructing the effective Hamiltonian from the Green's function is presented in Ref. [44]; for instance, see Eq. (40) of Ref. [43]. Specifically, the low-energy effective Hamiltonian is represented by

$$\begin{aligned} \tilde{\mathcal{H}}_\nu^{\text{eff}}(\mathbf{k}) &= \begin{pmatrix} \tilde{h}_\nu(\mathbf{k}) & \tilde{\Delta}_\nu(\mathbf{k}) \\ \tilde{\Delta}_\nu^\dagger(\mathbf{k}) & -\tilde{h}_\nu^\dagger(-\mathbf{k}) \end{pmatrix}, \\ \tilde{h}_\nu &= (\varepsilon_\nu + \gamma_\nu) \tilde{\sigma}_0 + \mathbf{m}_\nu \cdot \tilde{\boldsymbol{\sigma}}, \\ \tilde{\Delta}_\nu &= \psi_\nu i \tilde{\sigma}_y, \end{aligned} \quad (\text{B111})$$

where

$$\mathbf{m}_\nu = \sum_{\nu' \neq \nu} \frac{2\text{Re}[\psi_{\nu'\nu} \mathbf{d}_{\nu'\nu}^*] - i[\mathbf{d}_{\nu'\nu} \times \mathbf{d}_{\nu'\nu}^*]}{\varepsilon_\nu - \varepsilon_{\nu'}} \quad (\text{B112})$$

$$\gamma_\nu = \sum_{\nu' \neq \nu} \frac{|\psi_{\nu'\nu}|^2 + |\mathbf{d}_{\nu'\nu}|^2}{\varepsilon_\nu - \varepsilon_{\nu'}}, \quad (\text{B113})$$

which is also given as Eqs. (11) and (12) in the main text. We note that the pseudo-Zeeman field \mathbf{m}_ν and the correction in the kinetic energy γ_ν is proportional to Δ^2 .

APPENDIX C: RECURSIVE GREEN'S FUNCTION

We can deform the BdG Hamiltonian in Eq. (2) as

$$\begin{aligned} \tilde{H}(\mathbf{k}) &= \tilde{h}_0(\mathbf{k}_\parallel) + \tilde{t}_1(\mathbf{k}_\parallel) \exp\left(-i \frac{k_z c}{2}\right) + \tilde{t}_2(\mathbf{k}_\parallel) \exp(-ik_z c) \\ &\quad + \tilde{t}_1^\dagger(\mathbf{k}_\parallel) \exp\left(i \frac{k_z c}{2}\right) + \tilde{t}_2^\dagger(\mathbf{k}_\parallel) \exp(ik_z c), \end{aligned} \quad (\text{C1})$$

where \mathbf{k}_\parallel is the wave number (k_x, k_y) , and c is the lattice constant of the conventional unit cell in the z direction. Here \tilde{h}_0 and $\tilde{t}_{1(2)}$ are the intralayer element and the interlayer elements between the (next) nearest-neighbor layers of the Hamiltonian, respectively. When we employ a real space basis along the z direction, the Hamiltonian with n layers along the z direction is represented by

$$H_n = \frac{1}{2} \sum_{\mathbf{k}_\parallel} \tilde{C}_{n,\mathbf{k}_\parallel}^\dagger \tilde{H}_n(\mathbf{k}_\parallel) \tilde{C}_{n,\mathbf{k}_\parallel} \quad (\text{C2})$$

$$\tilde{H}_n(\mathbf{k}_\parallel) = \begin{pmatrix} \tilde{h}_0 & \tilde{t}_1 & \tilde{t}_2 & 0 \\ \tilde{t}_1^\dagger & \tilde{h}_0 & \tilde{t}_1 & \tilde{t}_2 \\ \tilde{t}_2^\dagger & \tilde{t}_1^\dagger & \tilde{h}_0 & \tilde{t}_1 \\ 0 & \tilde{t}_2^\dagger & \tilde{t}_1^\dagger & \tilde{h}_0 \\ & & & \vdots \end{pmatrix} \quad (\text{C3})$$

$$\tilde{C}_{n,\mathbf{k}_\parallel}^\dagger = (\tilde{C}_{1,\mathbf{k}_\parallel}^\dagger, \tilde{C}_{2,\mathbf{k}_\parallel}^\dagger, \dots, \tilde{C}_{n,\mathbf{k}_\parallel}^\dagger), \quad (\text{C4})$$

where

$$\begin{aligned} \tilde{C}_{j,\mathbf{k}_\parallel}^\dagger &= (c_{j,yz\uparrow,\mathbf{k}_\parallel}, c_{j,zx\uparrow,\mathbf{k}_\parallel}, c_{j,xy\uparrow,\mathbf{k}_\parallel}, c_{j,yz\downarrow,\mathbf{k}_\parallel}, c_{j,zx\downarrow,\mathbf{k}_\parallel}, c_{j,xy\downarrow,\mathbf{k}_\parallel}, \\ &\quad \times c_{j,yz\uparrow,-\mathbf{k}_\parallel}^\dagger, c_{j,zx\uparrow,-\mathbf{k}_\parallel}^\dagger, c_{j,xy\uparrow,-\mathbf{k}_\parallel}^\dagger, \\ &\quad \times c_{j,yz\downarrow,-\mathbf{k}_\parallel}^\dagger, c_{j,zx\downarrow,-\mathbf{k}_\parallel}^\dagger, c_{j,xy\downarrow,-\mathbf{k}_\parallel}^\dagger) \end{aligned} \quad (\text{C5})$$

is the creation operator of the quasi particles in the j th layer. We treat the n -layers system as the n' ($=n/2$) layers system by treating two adjacent original layers as a single layer. The Green's function of the $2n'$ layers system is given by $\tilde{G}^{n'}(z, \mathbf{k}_\parallel) = [z\tilde{I} - \tilde{H}_{2n'}(\mathbf{k}_\parallel)]^{-1}$, where \tilde{I} is the unit matrix and $z = \varepsilon + i\delta$. ε is a real frequency, and δ is an infinitesimal imaginary part. We define $\tilde{G}_{n'}^{n'}$ as the (n', n') component of $\tilde{G}^{n'}$. $\tilde{G}_{n'}^{n'}$ is a 24×24 matrix with the orbital-, spin-, particle-hole-, and layer-degrees of freedom. By taking the limit $n' \rightarrow \infty$ with the Möbius transformation, we obtain the top-surface Green's function for the semi-infinite system [41]: $\tilde{g}^s = \lim_{n' \rightarrow \infty} \tilde{G}_{n'}^{n'}$ which satisfies

$$\begin{aligned} \tilde{g}^s(\mathbf{k}_\parallel, z) &= [z\tilde{I} - \tilde{h}(\mathbf{k}_\parallel) - \tilde{t}^\dagger(\mathbf{k}_\parallel) \tilde{g}^s(\mathbf{k}_\parallel, z) \tilde{t}(\mathbf{k}_\parallel)]^{-1}, \\ \tilde{h} &= \begin{pmatrix} \tilde{h}_0 & \tilde{t}_1 \\ \tilde{t}_1^\dagger & \tilde{h}_0 \end{pmatrix}, \quad \tilde{t} = \begin{pmatrix} \tilde{t}_2 & 0 \\ \tilde{t}_1 & \tilde{t}_2 \end{pmatrix}. \end{aligned} \quad (\text{C6})$$

In the main text, h and t in Eq. (18) correspond to \tilde{h} and \tilde{t} , respectively.

APPENDIX D: ONE-DIMENSIONAL WINDING NUMBER

We discuss the (001) surface states of the chiral d -wave SC state in the single-band model by following Ref. [45]. We consider the BdG Hamiltonian, $\mathcal{H} = \frac{1}{2} \sum_{\mathbf{k}} \Psi_{\mathbf{k}}^\dagger H(\mathbf{k}) \Psi_{\mathbf{k}}$ with $\Psi_{\mathbf{k}}^\dagger = (c_{\mathbf{k}\uparrow}, c_{\mathbf{k}\downarrow}, c_{-\mathbf{k}\uparrow}^\dagger, c_{-\mathbf{k}\downarrow}^\dagger)$,

$$H(\mathbf{k}) = \begin{pmatrix} \epsilon(\mathbf{k}) & \Delta(\mathbf{k}) \\ \Delta^\dagger(\mathbf{k}) & -\epsilon^\dagger(-\mathbf{k}) \end{pmatrix}, \quad (\text{D1})$$

where $c_{\mathbf{k}s}$ is the annihilation operator for a momentum \mathbf{k} and a spin s . We consider the kinetic energy of the normal state as

$$\epsilon(\mathbf{k}) = \left[\frac{\hbar^2}{2m} (k_x^2 + k_y^2) - 2t_z(1 - \cos k_z) - \mu \right] \sigma_0. \quad (\text{D2})$$

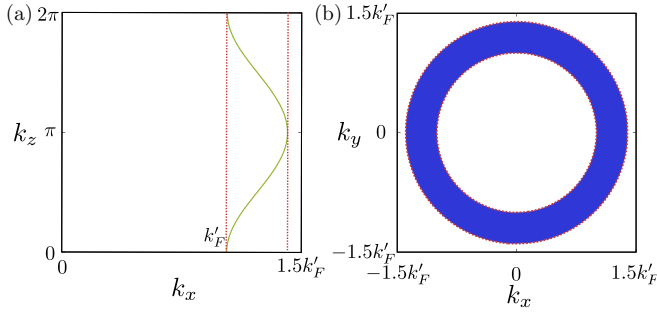


FIG. 8. (a) The k_z dependence of the Fermi surface of Eq. (D2) ($t_z = 0.1\mu$) on the k_x axis ($k'_F = \sqrt{2m\mu/\hbar^2}$). (b) The momentum range where the zero-energy surface states appear.

where t_z is the nearest-neighbor hopping for the c axis, m is the effective mass of electron in the xy plane, μ is the chemical potential. By employing a tight-binding approximation along z direction, we reproduce a cylindrical Fermi surface as shown in Fig. 8(a), where we choose $t_z = 0.1\mu$. The pair potential is given as

$$\begin{aligned}\Delta(\mathbf{k}) &= \Delta_0 \sin(k_z)(\bar{k}_x + i\bar{k}_y)i\sigma_2 \\ &= \Delta_0 \sin(k_z)e^{i\phi_{k_{\parallel}}}i\sigma_2\end{aligned}\quad (\text{D3})$$

where $\bar{k}_{x(y)} = k_{x(y)}/\sqrt{k_x^2 + k_y^2}$, $\phi_{k_{\parallel}} = \tan^{-1}(k_y/k_x)$, and $\mathbf{k}_{\parallel} = k_x\mathbf{e}_x + k_y\mathbf{e}_y$ with $\mathbf{e}_{x(y)}$ representing the unit vector along the $x(y)$ direction. The pair potential has sinusoidal dependence with respect to k_z and therefore has the line nodes at $k_z = 0$ and π . The Hamiltonian has particle-hole symmetry, $CH(\mathbf{k})C^{-1} = -H(-\mathbf{k})$ with $C = \sigma_0\tau_1K$ [45]. Here K is a complex conjugation operator and $\tau_{1,2,3}$ are Pauli matrices in the particle-hole space. By utilizing a local gauge transformation, $U_{\phi_{k_{\parallel}}} = e^{-i\frac{1}{2}\phi_{k_{\parallel}}\sigma_0\tau_3}$, we can see that the Hamiltonian has pseudo-time reversal symmetry, $U_{\phi_{k_{\parallel}}}^{\dagger}TU_{\phi_{k_{\parallel}}}H(\mathbf{k})U_{\phi_{k_{\parallel}}}^{\dagger}TU_{\phi_{k_{\parallel}}} = H(-\mathbf{k})$ with time reversal operator $T = i\sigma_2\tau_0K$. Then, the Hamiltonian has chiral symmetry that the Hamiltonian anticommutes with a chiral operator $\Gamma_{\phi_{k_{\parallel}}} = -iCU_{\phi_{k_{\parallel}}}^{\dagger}TU_{\phi_{k_{\parallel}}}$: $\{H(\mathbf{k}), \Gamma_{\phi_{k_{\parallel}}}\} = 0$. As a result, we can define a one-dimensional winding number w , which characterizes the topologically protected surface states at the (001) surface,

$$w(\mathbf{k}_{\parallel}) = \frac{i}{4\pi} \int dk_z \text{tr}[\Gamma_{\phi_{k_{\parallel}}} H^{-1}(\mathbf{k}) \partial_{k_z} H(\mathbf{k})]. \quad (\text{D4})$$

According to the bulk-boundary correspondence, the nonzero winding number at \mathbf{k}_{\parallel} guarantees the zero-energy surface states at \mathbf{k}_{\parallel} . Thus, when the winding number becomes nonzero in a finite range with respect to \mathbf{k}_{\parallel} , we obtain the flat-band zero-energy surface states at the (001) surface [46]. The Eq. (D4) can be rewritten as [46]

$$\begin{aligned}w(\mathbf{k}_{\parallel}) &= -\frac{1}{2} \sum_{\Delta'(k_z)=0} \text{sgn}[\partial_{k_z} \Delta'(k_z)] \cdot \text{sgn}[\epsilon(k_z, \mathbf{k}_{\parallel})] \\ &= -\frac{1}{2} [\text{sgn}[\epsilon(0, \mathbf{k}_{\parallel})] - \text{sgn}[\epsilon(\pi, \mathbf{k}_{\parallel})]].\end{aligned}\quad (\text{D5})$$

where $\Delta'(k_z) = \Delta_0 \sin(k_z)$. The summation is taken for k_z satisfying $\Delta'(k_z) = 0$. We clearly see that the winding number becomes nonzero in the momentum region where the signs of $\epsilon(0, \mathbf{k}_{\parallel})$ and $\epsilon(\pi, \mathbf{k}_{\parallel})$ are opposite. Namely, we obtain the flat-band zero-energy states in the momentum region enclosed by the nodal lines projected on the surface BZ as shown in Fig. 8(b). In the main text, we expect that the effective chiral d -wave SC originated from the E_g interorbital orbital pair potential can also host the surface states as the pure chiral d -wave SC.

Finally, we discuss the winding numbers for other candidate states in SRO: the (A) $s' + id_{x^2-y^2}$ -wave state [28], (B) $d_{x^2-y^2} + id_{xy(x^2-y^2)}$ -wave state [29–32], and (C) $s + id_{xy}$ -wave state [33,34] described by the pair potentials,

$$\begin{aligned}\Delta(\mathbf{k}) &= (\Delta_1 + i\Delta_2)i\sigma_2, \\ \Delta_1 &= \begin{cases} \Delta_R(\cos k_x + \cos k_y) & \text{for (A)} \\ \Delta_R(\cos k_x - \cos k_y) & \text{for (B)}, \\ \Delta_R & \text{for (C)} \end{cases} \\ \Delta_2 &= \begin{cases} \Delta_I(\cos k_x - \cos k_y) & \text{for (A)} \\ \Delta_I \sin k_x \sin k_y (\cos k_x - \cos k_y) & \text{for (B)}, \\ \Delta_I \sin k_x \sin k_y & \text{for (C)} \end{cases}\end{aligned}\quad (\text{D6})$$

which can be deformed as

$$\begin{aligned}\Delta(\mathbf{k}) &= \tilde{\Delta}_0(\mathbf{k}_{\parallel})e^{i\tilde{\phi}_{k_{\parallel}}}i\sigma_2, \\ \tilde{\Delta}_0(\mathbf{k}_{\parallel}) &= \sqrt{\Delta_1^2 + \Delta_2^2}, \quad \tilde{\phi}_{k_{\parallel}} = \tan^{-1}(\Delta_2/\Delta_1).\end{aligned}\quad (\text{D7})$$

The corresponding winding number can be evaluated by Eq. (D5) with replacing $\Delta'(k_z)$ with $\tilde{\Delta}_0(\mathbf{k}_{\parallel})$. Nevertheless,

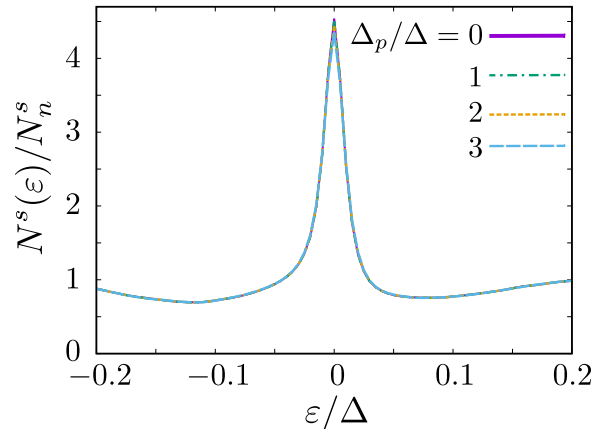


FIG. 9. The Δ_p dependence of the LDOS is plotted as a function of ϵ . There is the chiral E_u pair potential state at the top surface instead of the E_g interorbital pair potential. $\Delta = |t_z^{(xy,xy)}| \times 10^{-4}$.

since $\tilde{\Delta}_0(\mathbf{k}_{\parallel})$ never changes its sign with respect to k_z , we soon obtain $w(\mathbf{k}_{\parallel}) = 0$ irrelevant to \mathbf{k}_{\parallel} . Consequently, we can not expect the flat-band zero-energy states at the top surfaces of the $s' + id_{x^2-y^2}$ -wave, $d_{x^2-y^2} + ig_{xy(x^2-y^2)}$ -wave, and $s + id_{xy}$ -wave superconductors.

APPENDIX E: LDOS UNDER E_u SC STATE AT THE TOP SURFACE

In this Appendix, we show the stability of the zero-energy peak structure in the LDOS against the chiral E_u pair potential at the surface. Specifically, only at the top surface, we replace

the E_g interorbital pair potential as in Eq. (5) in the main text with

$$\hat{\Delta}_p = \begin{pmatrix} 0 & \bar{\Delta}_p \\ \bar{\Delta}_p & 0 \end{pmatrix}, \quad \bar{\Delta}_p = \Delta_p \bar{\lambda}_p, \\ \bar{\lambda}_p = \begin{pmatrix} i \sin k_y a & 0 & 0 \\ 0 & \sin k_x a & 0 \\ 0 & 0 & \sin k_x a + i \sin k_y a \end{pmatrix}, \quad (\text{E1})$$

where Δ_p is the magnitude of the pair potential. As shown in Fig. 9, the zero-energy peak structure remains robustly as long as Δ_p is varied within the order of the bulk pair potential Δ .

-
- [1] Y. Maeno, H. Hashimoto, K. Yoshida, S. Nishizaki, T. Fujita, J. G. Bednorz, and F. Lichtenberg, *Nature (London)* **372**, 532 (1994).
- [2] K. Ishida, H. Mukuda, Y. Kitaoka, K. Asayama, Z. Q. Mao, Y. Mori, and Y. Maeno, *Nature (London)* **396**, 658 (1998).
- [3] J. A. Duffy, S. M. Hayden, Y. Maeno, Z. Mao, J. Kulda, and G. J. McIntyre, *Phys. Rev. Lett.* **85**, 5412 (2000).
- [4] G. M. Luke, Y. Fudamoto, K. M. Kojima, M. I. Larkin, J. Merrin, B. Nachumi, Y. J. Uemura, Y. Maeno, Z. Q. Mao, Y. Mori *et al.*, *Nature (London)* **394**, 558 (1998).
- [5] J. Xia, Y. Maeno, P. T. Beyersdorf, and M. M. Fejer, and A. Kapitulnik, *Phys. Rev. Lett.* **97**, 167002 (2006).
- [6] T. Nomura and K. Yamada, *J. Phys. Soc. Jpn.* **69**, 3678 (2000).
- [7] M. Sato and M. Kohmoto, *J. Phys. Soc. Jpn.* **69**, 3505 (2000).
- [8] T. Takimoto, *Phys. Rev. B* **62**, R14641(R) (2000).
- [9] K. Kuroki, M. Ogata, R. Arita, and H. Aoki, *Phys. Rev. B* **63**, 060506(R) (2001).
- [10] T. Nomura and K. Yamada, *J. Phys. Soc. Jpn.* **71**, 404 (2002).
- [11] T. Nomura and K. Yamada, *J. Phys. Soc. Jpn.* **71**, 1993 (2002).
- [12] Y. Yanase and M. Ogata, *J. Phys. Soc. Jpn.* **72**, 673 (2003).
- [13] T. Nomura and K. Yamada, *J. Phys. Soc. Jpn.* **74**, 1818 (2005).
- [14] T. Nomura, D. S. Hirashima, and K. Yamada, *J. Phys. Soc. Jpn.* **77**, 024701 (2008).
- [15] S. Raghu, A. Kapitulnik, and S. A. Kivelson, *Phys. Rev. Lett.* **105**, 136401 (2010).
- [16] M. Tsuchiizu, Y. Yamakawa, S. Onari, Y. Ohno, and H. Kontani, *Phys. Rev. B* **91**, 155103 (2015).
- [17] L.-D. Zhang, W. Huang, F. Yang, and H. Yao, *Phys. Rev. B* **97**, 060510(R) (2018).
- [18] W.-S. Wang, C.-C. Zhang, F.-C. Zhang, and Q.-H. Wang, *Phys. Rev. Lett.* **122**, 027002 (2019).
- [19] Z. Wang, X. Wang, and C. Kallin, *Phys. Rev. B* **101**, 064507 (2020).
- [20] A. Pustogow, Y. Luo, A. Chronister, Y.-S. Su, D. A. Sokolov, F. Jerzembeck, A. P. Mackenzie, C. W. Hicks, N. Kikugawa, S. Raghu *et al.*, *Nature (London)* **574**, 72 (2019).
- [21] K. Ishida, M. Manago, K. Kinjo, and Y. Maeno, *J. Phys. Soc. Jpn.* **89**, 034712 (2020).
- [22] A. Chronister, A. Pustogow, N. Kikugawa, D. A. Sokolov, F. Jerzembeck, C. W. Hicks, A. P. Mackenzie, E. D. Bauer, and S. E. Brown, *Proc. Natl. Acad. Sci. USA* **118**, e2025313118 (2021).
- [23] A. N. Petsch, M. Zhu, M. Enderle, Z. Q. Mao, Y. Maeno, I. I. Mazin, and S. M. Hayden, *Phys. Rev. Lett.* **125**, 217004 (2020).
- [24] S. Ghosh, A. Shekhter, F. Jerzembeck, N. Kikugawa, D. A. Sokolov, M. Brando, A. P. Mackenzie, C. W. Hicks, and B. J. Ramshaw, *Nat. Phys.* **17**, 199 (2021).
- [25] D. F. Agterberg, *Nat. Phys.* **17**, 169 (2021).
- [26] S. Benhabib, C. Lupien, I. Paul, L. Berges, M. Dion, M. Nardone, A. Zitouni, Z. Q. Mao, Y. Maeno, A. Georges, L. Taillefer, and C. Proust, *Nat. Phys.* **17**, 194 (2021).
- [27] S. Ikegaya, S.-I. Suzuki, Y. Tanaka, and D. Manske, *Phys. Rev. Res.* **3**, L032062 (2021).
- [28] A. T. Rømer, D. D. Scherer, I. M. Eremin, P. J. Hirschfeld, and B. M. Andersen, *Phys. Rev. Lett.* **123**, 247001 (2019).
- [29] S. A. Kivelson, A. C. Yuan, B. Ramshaw, and R. Thomale, *npj Quantum Mater.* **5**, 43 (2020).
- [30] R. Willa, M. Hecker, R. M. Fernandes, and J. Schmalian, *Phys. Rev. B* **104**, 024511 (2021).
- [31] J. Clepkens, A. W. Lindquist, X. Liu, and H.-Y. Kee, *Phys. Rev. B* **104**, 104512 (2021).
- [32] A. C. Yuan, E. Berg, and S. A. Kivelson, *Phys. Rev. B* **104**, 054518 (2021).
- [33] J. Clepkens, A. W. Lindquist, and H.-Y. Kee, *Phys. Rev. Res.* **3**, 013001 (2021).
- [34] A. T. Rømer, P. J. Hirschfeld, and B. M. Andersen, *Phys. Rev. B* **104**, 064507 (2021).
- [35] A. Ramires and M. Sgrist, *Phys. Rev. B* **100**, 104501 (2019).
- [36] H. G. Suh, H. Menke, P. M. R. Brydon, C. Timm, A. Ramires, and D. F. Agterberg, *Phys. Rev. Res.* **2**, 032023(R) (2020).
- [37] S. Käser, H. U. R. Strand, N. Wentzell, A. Georges, O. Parcollet, and P. Hansmann, *Phys. Rev. B* **105**, 155101 (2022).
- [38] M. Sgrist and K. Ueda, *Rev. Mod. Phys.* **63**, 239 (1991).
- [39] R. Fittipaldi, R. Hartmann, M. T. Mercaldo, S. Komori, A. Bjørli, W. Kyung, Y. Yasui, T. Miyoshi, L. A. B. Olde Olthof *et al.*, *Nat. Commun.* **12**, 5792 (2021).
- [40] V. Grinenko, D. Das, R. Gupta, B. Zinkl, N. Kikugawa, Y. Maeno, C. W. Hicks, H. Klauss, M. Sgrist, and R. Khasanov, *Nat. Commun.* **12**, 3920 (2021).
- [41] A. Umerski, *Phys. Rev. B* **55**, 5266 (1997).
- [42] D. F. Agterberg, P. M. R. Brydon, and C. Timm, *Phys. Rev. Lett.* **118**, 127001 (2017).
- [43] P. M. R. Brydon, D. F. Agterberg, H. Menke, and C. Timm, *Phys. Rev. B* **98**, 224509 (2018).
- [44] J. W. F. Venderbos, L. Savary, J. Ruhman, P. A. Lee, and L. Fu, *Phys. Rev. X* **8**, 011029 (2018).
- [45] S. Kobayashi, Y. Tanaka, and M. Sato, *Phys. Rev. B* **92**, 214514 (2015).

- [46] M. Sato, Y. Tanaka, K. Yada, and T. Yokoyama, *Phys. Rev. B* **83**, 224511 (2011).
- [47] C.-R. Hu, *Phys. Rev. Lett.* **72**, 1526 (1994).
- [48] S. Kashiwaya and Y. Tanaka, *Rep. Prog. Phys.* **63**, 1641 (2000).
- [49] Y. Asano, Y. Tanaka, and S. Kashiwaya, *Phys. Rev. B* **69**, 134501 (2004).
- [50] Y. Tanaka and S. Kashiwaya, *Phys. Rev. Lett.* **74**, 3451 (1995).
- [51] L. J. Buchholtz and G. Zwicknagl, *Phys. Rev. B* **23**, 5788 (1981).
- [52] J. Hara and K. Nagai, *Prog. Theor. Phys.* **76**, 1237 (1986).
- [53] Y. Tanaka, M. Sato, and N. Nagaosa, *J. Phys. Soc. Jpn.* **81**, 011013 (2012).
- [54] S. Tamura, S. Kobayashi, L. Bo, and Y. Tanaka, *Phys. Rev. B* **95**, 104511 (2017).
- [55] S.-I. Suzuki, M. Sato, and Y. Tanaka, *Phys. Rev. B* **101**, 054505 (2020).
- [56] Y. Fukaya, S. Tamura, K. Yada, Y. Tanaka, P. Gentile, and M. Cuoco, *Phys. Rev. B* **97**, 174522 (2018).
- [57] Y. Yanase, *J. Phys. Soc. Jpn.* **82**, 044711 (2013).
- [58] G. Khalsa, B. Lee, and A. H. MacDonald, *Phys. Rev. B* **88**, 041302(R) (2013).
- [59] I. A. Firmo, S. Lederer, C. Lupien, A. P. Mackenzie, J. C. Davis, and S. A. Kivelson, *Phys. Rev. B* **88**, 134521 (2013).
- [60] R. Sharma, S. D. Edkins, Z. Wang, A. Kostina, C. Sowe, Y. Maeno, A. P. Mackenzie, J. C. Seamus Davis, and V. Madhavan, *Proc. Natl. Acad. Sci. USA* **117**, 5222 (2020).
- [61] S.-I. Suzuki, S. Ikegaya, and A. A. Golubov, *Phys. Rev. Res.* **4**, L042020 (2022).
- [62] A. Damascelli, D. H. Lu, K. M. Shen, N. P. Armitage, F. Ronning, D. L. Feng, C. Kim, Z.-X. Shen, T. Kimura, Y. Tokura, Z. Q. Mao, and Y. Maeno, *Phys. Rev. Lett.* **85**, 5194 (2000).
- [63] C. A. Marques, L. C. Rhodes, R. Fittipaldi, V. Granata, C. Yim, R. Buzio, A. Gerbi, A. Vecchione, A. W. Rost, and P. Wahl, *Adv. Mater.* **33**, 2100593 (2021).
- [64] Y. Takagaki and K. H. Ploog, *Phys. Rev. B* **60**, 9750 (1999).
- [65] K. Tsuchikawa, N. Yoshida, Y. Tanaka, S. Kashiwaya, J. Inoue, and Y. Takagaki, *Physica C: Superconductivity* **357-360**, 1588 (2001).
- [66] K. Tsuchikawa, N. Yoshida, Y. Tanaka, S. Kashiwaya, J. Inoue, and Y. Takagaki, *Physica C: Superconductivity* **362**, 224 (2001).
- [67] W. J. Herrera, J. V. Niño, and J. J. Giraldo, *Phys. Rev. B* **71**, 094515 (2005).
- [68] Y. Tanaka, Y. V. Nazarov, A. A. Golubov, and S. Kashiwaya, *Phys. Rev. B* **69**, 144519 (2004).
- [69] Y. Tanaka, Y. V. Nazarov, and S. Kashiwaya, *Phys. Rev. Lett.* **90**, 167003 (2003).
- [70] Y. Tanaka and S. Kashiwaya, *Phys. Rev. B* **70**, 012507 (2004).
- [71] M. Roig, A. T. Rømer, A. Kreisel, P. J. Hirschfeld, and B. M. Andersen, *Phys. Rev. B* **106**, L100501 (2022).
- [72] A. T. Rømer, T. A. Maier, A. Kreisel, P. J. Hirschfeld, and B. M. Andersen, *Phys. Rev. Res.* **4**, 033011 (2022).